Monthly Notices
of the
ROYAL ASTRONOMICAL SOCIETY

MNRAS **475,** 3700–3729 (2018)
Advance Access publication 2018 January 5

doi:10.1093/mnras/stx3346

Timing the formation and assembly of early-type galaxies via spatially resolved stellar populations analysis

Ignacio Martín-Navarro,[1,2★] Alexandre Vazdekis,[3,4] Jesús Falcón-Barroso,[3,4] Francesco La Barbera,[5] Akın Yıldırım[6] and Glenn van de Ven[2,7]

[1] *University of California Observatories, 1156 High Street, Santa Cruz, CA 95064, USA*
[2] *Max-Planck Institut für Astronomie, Konigstuhl 17, D-69117 Heidelberg, Germany*
[3] *Instituto de Astrofísica de Canarias, E-38200 La Laguna, Tenerife, Spain*
[4] *Departamento de Astrofísica, Universidad de La Laguna, E-38205 La Laguna, Tenerife, Spain*
[5] *INAF - Osservatorio Astronomico di Capodimonte, Napoli, Italy*
[6] *Max-Planck Institut für Astrophysics, Karl-Schwarzschild-Str. 1, D-85741 Garching, Germany*
[7] *European Southern Observatory, Karl-Schwarzschild-Str. 2, D-85748 Garching b. München, Germany*

Accepted 2017 December 18. Received 2017 December 1; in original form 2017 October 12

ABSTRACT

To investigate star formation and assembly processes of massive galaxies, we present here a spatially resolved stellar population analysis of a sample of 45 elliptical galaxies (Es) selected from the Calar Alto Legacy Integral Field Area survey. We find rather flat age and [Mg/Fe] radial gradients, weakly dependent on the effective velocity dispersion of the galaxy within half-light radius. However, our analysis shows that metallicity gradients become steeper with increasing galaxy velocity dispersion. In addition, we have homogeneously compared the stellar population gradients of our sample of Es to a sample of nearby relic galaxies, i.e. local remnants of the high-z population of *red nuggets*. This comparison indicates that, first, the cores of present-day massive galaxies were likely formed in gas-rich, rapid star formation events at high redshift ($z \gtrsim 2$). This led to radial metallicity variations steeper than observed in the local Universe, and positive [Mg/Fe] gradients. Secondly, our analysis also suggests that a later sequence of minor dry mergers, populating the outskirts of early-type galaxies (ETGs), flattened the pristine [Mg/Fe] and metallicity gradients. Finally, we find a tight age–[Mg/Fe] relation, supporting that the duration of the star formation is the main driver of the [Mg/Fe] enhancement in massive ETGs. However, the star formation time-scale alone is not able to fully explain our [Mg/Fe] measurements. Interestingly, our results match the expected effect that a variable stellar initial mass function would have on the [Mg/Fe] ratio.

Key words: galaxies: abundances – galaxies: elliptical and lenticular, cD – galaxies: evolution – galaxies: formation – galaxies: stellar content.

1 INTRODUCTION

The hierarchical assembly of galaxies is a direct consequence of the favoured Λcold dark matter (ΛCDM) interpretation of the Universe. Structures within this paradigm grow via gravitational instabilities, in remarkable agreement with the observed large-scale structure of the Universe (e.g. Geller & Huchra 1989; Hernquist et al. 1996; Davé et al. 1999; Colless et al. 2001; Cole et al. 2005; Springel et al. 2005; Springel, Frenk & White 2006). Given the initial conditions provided by the cosmic microwave background (de Bernardis et al. 2000; Hinshaw et al. 2013; Planck Collaboration XVI 2014), the later evolution of structures is mostly driven by the dark matter gravitational field (White 1976; Frenk et al. 1988; Bond, Kofman & Pogosyan 1996), whose dynamics is well described by Newtonian gravity (Adamek et al. 2013).

Understanding the formation and evolution of galaxies, however, is a more complex task, as cosmological effects are generally overshadowed by baryonic processes. The evolution of the colour–magnitude relation (Bower, Lucey & Ellis 1992; Ellis et al. 1997; van Dokkum et al. 2000; van Dokkum & Franx 2001; Blakeslee et al. 2003; Bernardi et al. 2005) or the tight scaling relations between stellar population properties and galaxy mass (Faber 1973; Peletier 1989; Worthey, Faber & Gonzalez 1992; Bender, Burstein & Faber 1993; Trager et al. 2000a; Thomas et al. 2005) seem to question the hierarchical nature of the ΛCDM Universe. Ultimately, these difficulties to reconcile simulations and observations of galaxies arise from numerically unresolvable physical scales.

★ E-mail: imartinn@ucsc.edu

Cosmological simulations including coupling between electromagnetic fields and baryonic matter, stellar physics and even parsec-scale star formation are not yet feasible (see e.g. Baugh 2006). Thus, all these processes are usually simplified, using analytic recipes tuned up to match observations (e.g. Rees & Ostriker 1977; White & Frenk 1991; Kauffmann, White & Guiderdoni 1993; Somerville & Primack 1999; De Lucia & Blaizot 2007; De Lucia et al. 2012; Guo et al. 2016).

Arguably, the most paradigmatic example of the tension between cosmological simulations and actual observations is the apparent downsizing of nearby galaxies, which become older, more metal rich and formed more rapidly with increasing galaxy mass (Trager et al. 2000a; Thomas et al. 2005; Gallazzi et al. 2005, 2006; Yamada et al. 2006; Kuntschner et al. 2010; McDermid et al. 2015). Naively, and supported by the first cosmologically motivated numerical simulations, one would expect that massive galaxies in a ΛCDM Universe form through successive mergers of smaller galaxies. This would lead to young massive galaxies at $z \sim 0$, in sharp contrast with observations. To overcome this so-called over-cooling problem, feedback from the central super-massive black hole is usually invoked (e.g. Di Matteo, Springel & Hernquist 2005; De Lucia et al. 2006; Vogelsberger et al. 2014; Schaye et al. 2015).

Among all the observables that hold information about numerically unresolved scales, the overabundance of α-elements compared to iron-peak elements, i.e. the [α/Fe] ratio, stands as one of the most relevant. Under the standard interpretation, the [α/Fe] ratio is set by the time delay between core-collapse and Type Ia supernovae (SNe) (Tinsley 1979; Vazdekis et al. 1996; Thomas, Greggio & Bender 1999). The bulk of α-elements is produced in short-lived core-collapse SN, whereas the amount of iron-peak elements accumulates as Type Ia SNe keep polluting the interstellar medium in scales of a few Gyr. Therefore, the longer star formation lasts in a galaxy, the more iron is produced, and the lower is the observed [α/Fe] ratio. The fact that massive nearby galaxies exhibit enhanced [α/Fe] has been then interpreted as a consequence of a rapid formation process (Peletier 1989; Worthey, Faber & Gonzalez 1992; Thomas et al. 2005; de La Rosa et al. 2011; Conroy, Graves & van Dokkum 2014; Greene et al. 2015; McDermid et al. 2015).

However, whether this standard picture is enough to explain the observed properties of galaxies remains unclear. Segers et al. (2016) have recently claimed that feedback from active galactic nuclei solving the over-cooling problem explains also their enhanced [α/Fe] ratios, as star formation is rapidly quenched in massive galaxies. Such scenario seems to be supported by the relation between black holes and star formation (Martín-Navarro et al. 2016; Terrazas et al. 2016), and by the star formation histories of nearby galaxies (de La Rosa et al. 2011; McDermid et al. 2015). In contrast, it has also been suggested that a variable stellar initial mass function (IMF) might be necessary to explain the observed [α/Fe] dependence on galaxy mass (Arrigoni et al. 2010; Gargiulo et al. 2015; De Lucia, Fontanot & Hirschmann 2017; Fontanot et al. 2017). The impact of a variable IMF in the interpretation of the [α/Fe] ratio (Martín-Navarro 2016) has to be carefully considered given the empirical relation between IMF slope and galaxy mass (Cenarro et al. 2003; Treu et al. 2010; Thomas et al. 2011; Cappellari et al. 2012; Ferreras et al. 2013; La Barbera et al. 2013; Conroy et al. 2014; Spiniello et al. 2014). Moreover, IMF may also vary in time, as expected from observations, both locally and at high z (Vazdekis et al. 1996, 1997; van Dokkum 2008; Wang & Dai 2011; Weidner et al. 2013; Ferreras et al. 2015; Martín-Navarro et al. 2015b).

Understanding whether the abundance pattern probes the formation time-scale of a galaxy, or whether it is set by the (time-varying) high-mass end of the IMF, needs for detailed stellar population analysis. The relatively simple star formation histories of early-type galaxies (ETGs) make them ideal benchmark for stellar population studies. Dominating the high-mass end of the galaxy mass function (Bell et al. 2003), ETGs are expected to be among the most strongly AGN-quenched objects (Schawinski et al. 2007), exhibiting also the strongest IMF variations (van Dokkum & Conroy 2010) and highest [α/Fe] ratios (Thomas et al. 2005).

1.1 Stellar population gradients

The aforementioned relation between galaxy mass (or stellar velocity dispersion) and [α/Fe] is observationally well established for ETGs (Faber 1973; Peletier 1989; Worthey, Faber & Gonzalez 1992; Trager et al. 2000a; Thomas et al. 2005; Graves, Faber & Schiavon 2009a,b; Conroy, Graves & van Dokkum 2014; Walcher et al. 2015). However, these studies were focused on the global properties of ETGs, i.e. comparing quantities integrated over a fixed radial aperture. A few studies have taken a step forward analysing the radial [α/Fe] gradients in different ETG samples. Mehlert et al. (2003) analysed a sample of 35 ETGs in the Coma cluster and found that, on average, [α/Fe] gradients were flat. This was later confirmed by Sánchez-Blázquez et al. (2007), who studied the radial stellar population gradients of 11 ETGs covering a wide range of masses, although individual galaxies could show slightly positive or negative gradients. Because of the absence of strong positive [α/Fe] gradients, Sánchez-Blázquez et al. (2007) claimed that the properties of stellar populations in ETGs are not compatible in a purely outside-in collapse (Pipino & Matteucci 2004; Pipino, Matteucci & Chiappini 2006). Conversely, Sánchez-Blázquez et al. (2007) suggested that the correlation between structural parameters (in particular a_4, which quantifies isophotal deviations from a perfect ellipse) and stellar population gradients was a signature of merger driven formation scenario for ETGs. Spatially unresolved studies also show clear relations between galaxy structure and stellar population properties (Vazdekis, Trujillo & Yamada 2004). Similar trends as those described by Sánchez-Blázquez et al. (2007) were also found by Kuntschner et al. (2010) studying 48 Spectroscopic Areal Unit for Research on Optical Nebulae ETGs, and later revisited by McDermid et al. (2015) with the larger ATLAS^{3D} sample. Kuntschner et al. (2010) proposed that the observed relation between galaxy mass and [α/Fe] is due to metal-rich, young and mildly [α/Fe]-enhanced stellar populations, which become more prominent in low-mass ETGs. In agreement with a time-scale-dependent origin for the abundance pattern, these young and no [α/Fe]-enhanced stellar populations can also be seen in extreme kinematically decoupled components (Kleineberg, Sánchez-Blázquez & Vazdekis 2011), although it is not a common feature (Kuntschner et al. 2010).

In this paper we observationally address the origin of the stellar population gradients within ETGs by studying the two-dimensional age, metallicity, and [Mg/Fe] maps of 45 ETGs drawn from the Calar Alto Legacy Integral Field Area (CALIFA) sample (Sánchez et al. 2012; Walcher et al. 2014). In addition, we trace back the evolution of the stellar population gradients by comparing our CALIFA galaxies to a sample of massive relic galaxies (Yıldırım et al. 2017), discussing the implications for the evolutionary paths of ETGs. The outline of this paper is as follows. Data and sample are presented in Section 2. The ingredients of the stellar population modelling are presented in Section 3, and the analysis is detailed in Section 4. The results presented in Section 5 are discussed in Section 6. Finally, the conclusions of the paper are summarized in Section 7.

2 DATA AND SAMPLE SELECTION

Our analysis is based on the CALIFA survey (Sánchez et al. 2012) intended to observe a diameter-selected sample of nearby galaxies with the PMAS/PPak integral-field spectrograph (Verheijen et al. 2004; Roth et al. 2005; Kelz et al. 2006). Due to its wider wavelength coverage, from 3700 to 7000 Å (rest-frame), our analysis uses the V500 CALIFA setup, which provides an intermediate spectral resolution of 6 Å. The hexagonal CALIFA field of view covers $\sim$1.3 arcmin^2, with 1 arcsec^2 spaxel size. The exposure time was fixed to 900 s for the V500 setup, and allows us to typically reach up to 1 R_e (see Section 4).

Our preliminary sample encompassed every ETG both from the CALIFA mother sample (Walcher et al. 2014) and from the extended CALIFA sample presented in Sánchez et al. (2016). S0 were excluded from the analysis since they may represent an intermediate galaxy type, whose gaseous and stellar population properties are distinct from elliptical galaxies (Es) (e.g. Temi, Brighenti & Mathews 2009; Kuntschner et al. 2010; Sarzi et al. 2010, 2013; Amblard et al. 2014). However, some confusion between Es and S0s is expected for the latest morphological types in our sample. In Section 5.2 we discuss the impact of morphological subtypes on our results.

We found a strong systematic artefact at a rest-frame wavelength of $\lambda \sim 5460$Å. Since we were interested on the radial variations of the stellar population properties, we had to apply a redshift cut to our sample of elliptical galaxies to ensure that our analysis was not affected by this systematic. Therefore, our final sample consisted only of those Es within the CALIFA survey with redshift $z < 0.026$, 45 in total. The criterion for this redshift limit, based on the details of our stellar population analysis, is further explained in Section 4.1.

Effective velocity dispersions in our sample, measured within half R_e, range from $\sigma \sim 150$ to $\sigma \sim 350$ km s^{-1}, with a median value of $\sigma = 217$ km s^{-1}. According to Walcher et al. (2014), this translates to a median stellar mass of $\sim 10^{11}$ M$_\odot$, mass range where the CALIFA sample is representative of the local population of galaxies. In Fig. 1 we show the classical relation between Mg*b* line-strength and stellar velocity dispersion for our 45 Es. The basic properties of the sample are listed in Table 1.

For comparison, we also re-analyse the sample of massive compact relic galaxies presented in Yıldırım et al. (2017). These objects were also observed using the PMAS/PPak integral-field spectrograph, with the same instrumental setup as the V500 CALIFA data. This sample of nearby *red nuggets* (see Section 6.1) consists of 14 galaxies with a typical velocity dispersion of $\sigma \sim 275$ km s^{-1}. Their individual kinematical and stellar population properties are fully described in Yıldırım et al. (2017).

3 MILES ALPHA-ENHANCED MODELS

To study the stellar population properties in our sample of galaxies, we compared our integral-field spectroscopic data to the [α/Fe]-variable MILES stellar population synthesis models (Vazdekis et al. 2010, 2015). These new set of models were built by combining the theoretical response functions of Coelho et al. (2005, 2007) with the MILES stellar library (Sánchez-Blázquez et al. 2006), taking into account the [Mg/Fe] determination for the individual MILES stars (Milone, Sansom & Sánchez-Blázquez 2011). The stellar spectra were first used to populate, in a consistent way, solar-scaled and [α/Fe]-enhanced BaSTi isochrones (Pietrinferni et al. 2004, 2006). Later, the resulting single stellar population models were [α/Fe]-corrected using the theoretical response functions.

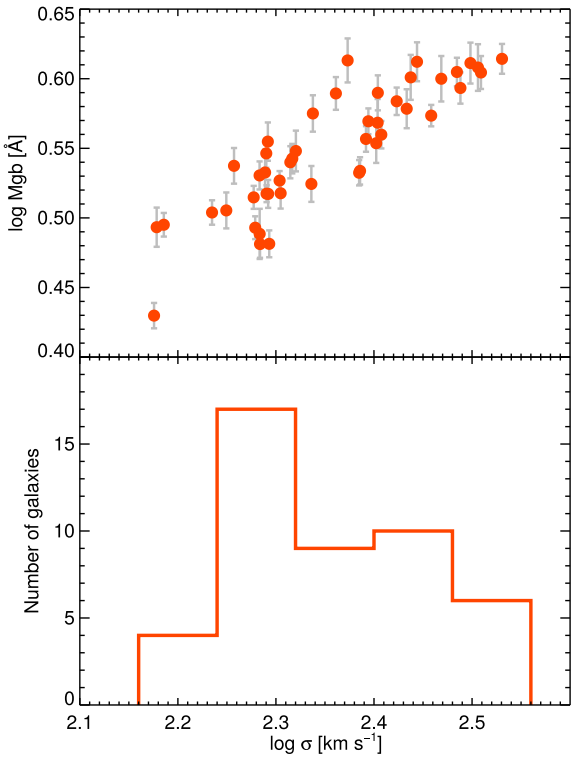

Figure 1. Mg*b*–σ relation. The top panel shows the measured Mg*b* line-strength (convolved to a common $\sigma = 350$) as a function of the effective velocity dispersion at 0.5 R_e for our sample of galaxies. The bottom panel shows the σ distribution for the 45 objects in the sample. The median value is $\sigma = 217$ km s^{-1}, or conversely, 9.8×10^{10} M$_\odot$ (Walcher et al. 2014).

The [α/Fe]-variable MILES models cover a wide range of ages, from 0.03 to 14 Gyr, as well as nominal metallicities from -2.27 to $+0.40$ dex. In addition, the models allow for [α/Fe] variations from 0.0 to +0.4 dex. Given the weak dependence of the selected spectral features on the IMF slope, we assumed a universal Kroupa-like IMF shape (Kroupa 2001, 2002).

Note that all α-elements are varied simultaneously in the [α/Fe]-variable MILES models, and therefore, the interpretation of the measured abundance pattern should be done carefully. Since our analysis is based on Fe and Mg optical features (see Section 4.1), we are only sensitive to the [Mg/Fe] ratio. However, if a different approach is followed (e.g. full spectral fitting) the resulting [α/Fe] value would be determined by the average effect of all α-elements on the analysed spectrum. Since elemental abundances vary from galaxy to galaxy, the same *average* [α/Fe] could be measured in two galaxies with a completely different partition of individual α-elements. This is particularly important when studying wavelengths bluewards than $\lambda \sim 4500$Å (Vazdekis et al. 2015). Similarly, when applying the [α/Fe]-variable MILES models to optical features sensitive to different elements such as Mg, Ca, or Ti, one could obtain different answers for each line/element.

4 ANALYSIS

In order to make full use of the CALIFA integral-field spectroscopy, we derived two-dimensional maps of all measured quantities. Data cubes were spatially binned using the Voronoi tessellation described in Cappellari & Copin (2003) to a common signal-to-noise ratio of 60 per Å.

Table 1. Basic properties of our sample of Es. Morphologies, effective radii, and ellipticity (ϵ) are those of Falcón-Barroso et al. (2017). Stellar masses were calculated by Walcher et al. (2014), and the effective velocity dispersions at half R_e were measured over the same CALIFA cubes used for the stellar population analysis (see Section 4).

Galaxy	Morphology	$M_\star$ [log $M_\odot$]	$\sigma_{0.5R_e}$ [km s^{-1}]	R_e [arcsec]	ϵ
NGC 0155	E1	10.8	177.5	15.8	0.14
NGC 0364	E7	10.8	229.7	15.8	0.27
NGC 0499	E5	11.1	277.9	21.3	0.32
NGC 0529	E4	11.0	247.9	12.6	0.09
NGC 0731	E1	10.7	171.7	11.4	0.07
NGC 0938	E3	10.7	192.2	13.8	0.25
NGC 0962	E3	10.9	180.8	13.8	0.22
NGC 1026	E2	10.7	206.4	17.4	0.24
NGC 1060	E3	11.4	322.9	27.3	0.18
NGC 1132	E6	11.1	252.5	32.8	0.40
NGC 1349	E6	11.0	209.1	17.0	0.11
NGC 1361	E5	10.6	194.5	16.2	0.32
NGC 1656	E6	10.5	149.8	17.4	0.44
NGC 2513	E2	11.2	307.7	26.5	0.26
NGC 2592	E4	10.5	236.1	9.9	0.21
NGC 2880	E7	10.5	153.3	18.2	0.35
NGC 2918	E6	11.2	243.1	12.2	0.30
NGC 3158	E3	11.5	339.3	32.4	0.18
NGC 3615	E5	11.3	287.3	15.4	0.41
NGC 4874	E0	11.3	273.8	55.0	0.23
NGC 5029	E6	11.3	271.2	25.3	0.39
NGC 5198	E1	10.8	217.6	16.2	0.12
NGC 5216	E0	10.4	150.8	20.1	0.32
NGC 5485	E5	10.7	195.0	31.6	0.32
NGC 5513	E6	11.0	189.3	15.8	0.44
NGC 5546	E3	11.3	320.6	17.4	0.12
NGC 5557	E4	11.3	255.5	24.5	0.20
NGC 5580	E2	10.6	195.7	15.0	0.13
NGC 5598	E6	10.9	192.0	9.10	0.32
NGC 5623	E7	10.7	294.2	15.4	0.32
NGC 5642	E5	11.0	246.5	18.6	0.38
NGC 5684	E3	10.8	192.0	17.8	0.27
NGC 5689	E6	10.9	190.0	17.0	0.75
NGC 5928	E4	10.9	201.2	15.8	0.31
NGC 5966	E4	10.8	201.7	18.6	0.38
NGC 6020	E4	10.7	207.3	19.0	0.30
NGC 6021	E5	10.9	216.8	9.50	0.27
NGC 6125	E1	11.1	253.4	21.7	0.04
NGC 6411	E4	10.9	195.1	34.0	0.35
NGC 6515	E3	11.0	195.9	19.0	0.34
NGC 7550	E4	11.2	242.5	24.5	0.09
NGC 7562	E4	11.2	264.9	20.9	0.32
NGC 7619	E3	11.3	305.2	35.6	0.17
UGC 05771	E6	11.1	253.3	12.6	0.32
UGC 10097	E5	11.3	315.0	14.6	0.17

To derive the stellar population properties within our Voronoi maps, we first needed to calculate the radial velocity (V) and σ of each spectra along the maps. We made use of the pipeline developed by Falcón-Barroso et al. (2017), which is fully detailed in their section 4. In summary, V and σ were derived using the Penalized Pixel-Fitting method (pPXF) (Cappellari & Emsellem 2004; Cappellari 2017), without including higher Gauss–Hermite terms. pPXF was fed with stellar templates from the Indo–US Library (Valdes et al. 2004), carefully selected to minimize template mismatch systematics (Falcón-Barroso et al. 2017). Once the kinematics of each spectra was measured, we corrected them for nebular emission using the Gas AND Absorption Line Fitting algorithm (GANDALF; Sarzi et al. 2006).

4.1 Stellar populations

We measured the stellar population properties using standard line-strength analysis. We used the Cervantes & Vazdekis (2009) definition of the Hβ_o index, combined with the Fe 4383 (Worthey et al. 1994), Fe 5015 (Worthey et al. 1994), Fe 5270 (Burstein et al. 1984), and Mgb (Burstein et al. 1984) standard line indices. Note that the only α-element measurable in CALIFA is Mg. Thus, when

analysing and discussing the abundance pattern in our data we explicitly used [Mg/Fe], but not the more general [α/Fe]. The [α/Fe]-variable MILES models can in principle be used to constrain other α-elements.

As described in Section 2, the presence of a systematic feature in the data forced us to apply a redshift cut to our sample. In order to maximize the number of galaxies in the final sample, we decided not to include the Fe 5335 spectral feature (our reddest metallic indicator) in the analysis (see details in Appendix A). This allowed us to study all galaxies with redshift $z < 0.026$. For larger redshifts, the systematic started to affect the Fe 5270 index definition. Notice that we also avoided the use of the strong NaD absorption lines, as it depends, not only on metallicity, but also strongly on the IMF slope and on the [Na/Fe] abundance (Spiniello et al. 2012; La Barbera et al. 2017).

Our stellar population modelling consisted therefore of three free parameters, namely age, metallicity ([M/H]), and [Mg/Fe], to be constrained with the five line-strength indices listed above. Stellar population properties were measured using the *emcee* Bayesian Markov chain Monte Carlo sampler (Foreman-Mackey et al. 2013). In practice, each walker tried to maximize the following likelihood function:

$$\ln(\boldsymbol{I}|\text{age}, [M/H], [\text{Mg/Fe}]) = -\frac{1}{2}\sum_n \left[\frac{(I_n - M_n)^2}{\sigma_n^2} - \ln\frac{1}{\sigma_n^2}\right]$$

where I_n, M_n and σ_n are the observed line-strength, model value, and error of our five indices, respectively. We assumed flat priors for the three free parameters. Model predictions M_n were calculated at the measured velocity dispersion of each spectrum. In such a way, we avoid degrading the resolution of the spectra, making full use of their information. We assume a constant resolution for the CALIFA data, with an instrumental FWHM=6 Å. Line-strength predictions were obtained by convolving MILES SSP models ($\text{FWHM}_{\text{MILES}} = 2.51$Å; Falcón-Barroso et al. 2011b) with a Gaussian kernel whose FWHM depends on the measured velocity dispersion for that particular radial bin (FWHM_{gal}, Section 4):

$$\text{FHWM}^2_{\text{ker}} = \text{FHWM}^2_{\text{CALIFA}} + \text{FHWM}^2_{\text{gal}} - \text{FHWM}^2_{\text{MILES}}.$$

A typical corner plot is shown in Fig. 2, where the degeneracies among age, metallicity, and [Mg/Fe] are partially broken. We use the median of the posterior distributions as our best-fitting solutions (red solid lines in Fig. 2) and 1σ uncertainties correspond to the 16th and 84th percentiles.

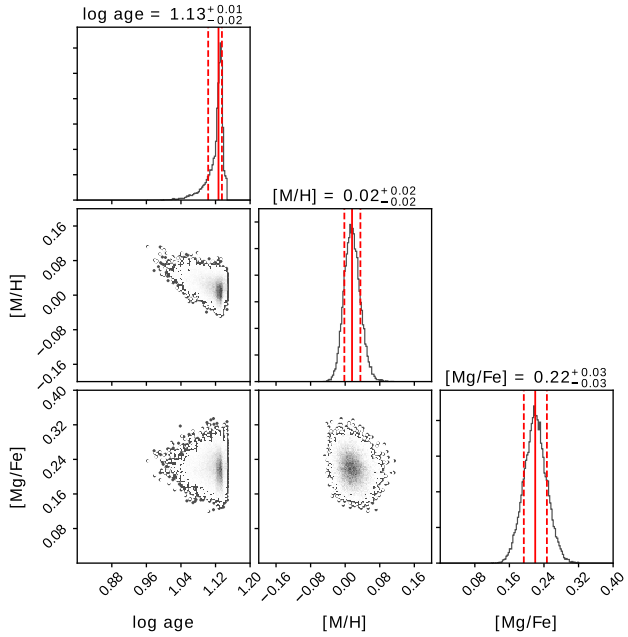

Figure 2. Example of a corner plot produced by our stellar populations fitting code, in this case for the galaxy NGC 7619. The cloud of points indicates the posterior distributions, while red lines mark the best-fitting (solid line) and 1σ confidence intervals (dashed lines). We are capable of breaking the degeneracies between the different stellar population parameters for a typical signal-to-noise ratio of ~60 per Å.

5 RESULTS

After the analysis of the CALIFA data cubes, for each galaxy in our sample we had a map of V, σ, age, metallicity, and [Mg/Fe]. As an example, the case of NGC 7619 is shown in Fig. 3, and the rest of maps can be found in Appendix C.

5.1 Global scaling relations

First, we analysed the relation between integrated stellar population properties and velocity dispersion. In Fig. 4 we show how age, metallicity, and [Mg/Fe] change as a function of the effective $\sigma_{0.5R_e}$. From left to right, the stellar population properties were measured over an integrated aperture of one tenth, one fourth, and half R_e. On each panel, the solid line indicates the best-fitting σ relation at $R_e/4$.

As expected, we found old stellar populations at all radii, with the scatter suggesting the presence of small fractions of younger populations. As indicated in the Introduction, this apparent *downsizing* is robustly supported by numerous observational studies (e.g. Trager et al. 2000a; Thomas et al. 2005; Sánchez-Blázquez et al. 2006; Kuntschner et al. 2010; McDermid et al. 2015), challenging a pure hierarchical assembly of massive ETGs. Residual recent star formation as seen in the inner regions of our sample is needed to explain the scatter of age-sensitive spectral features in the infrared (Falcón-Barroso et al. 2011a), in the optical (Trager et al. 2000b), and in the ultraviolet (Vazdekis et al. 2016).

Thomas et al. (2005) suggested that the Mgb–σ relation (top panel in Fig. 1) is mainly driven by an increase in metallicity with increasing galaxy σ. Although the physical origin of this relation is still under debate (Keller, Wadsley & Couchman 2016; Bower et al. 2017), it is clear from Fig. 4 that galaxies with higher σ exhibit higher metallicities. The distribution of [M/H] measurements clearly moves towards lower values as we probe the most external regions of our Es, indicating a negative metallicity gradients in our sample. This was already noticed by the early studies of Mehlert et al. (2003), Sánchez-Blázquez et al. (2007), and Spolaor et al. (2009), and it is usually understood as an imprint of the early gas collapse, later shaped by mergers.

Finally, the [Mg/Fe] trends as a function of σ and galactocentric distance are also shown in Fig. 4. We did find the expected enhancement in [Mg/Fe] with increasing sigma σ. Interestingly, and contrary to the behaviour of metallicity, there is not a clear trend with radius. The [Mg/Fe] enhancement of the inner regions is also observed beyond half R_e. This is in agreement with previous studies (Peletier et al. 1999; Mehlert et al. 2003; Sánchez-Blázquez et al. 2007; Kuntschner et al. 2010), and suggests a fundamental difference between the development of metallicity and abundance pattern gradients within ETGs.

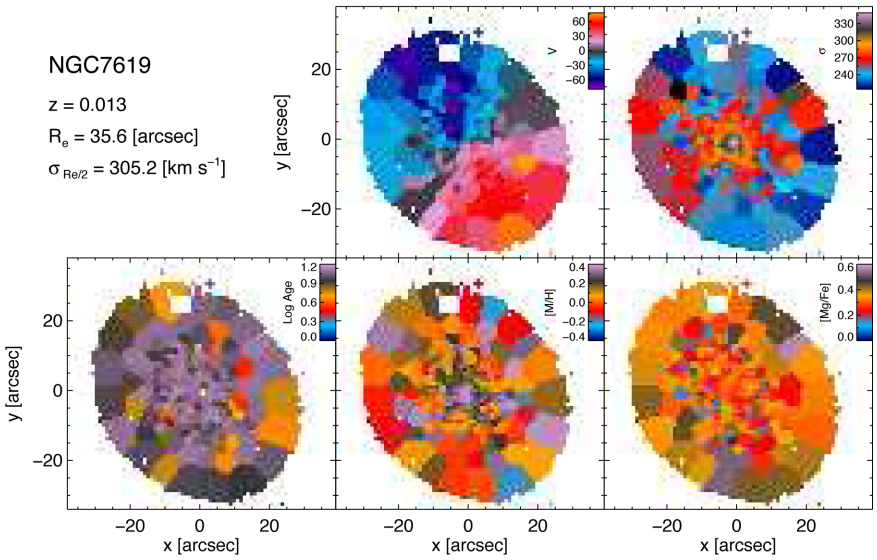

Figure 3. Kinematical and stellar population parameters measured for NGC 7619. From top to bottom and left to right we show here the velocity, σ, log age, [M/H], and [Mg/Fe] maps. The redshift, R_e, and effective σ are also indicated. There is a clear hint of rotation, as well as a radially declining σ profile. Ages are very old through all the galaxy, and the metallicity decreases outwards. The [Mg/Fe] maps show a mild positive radial gradient.

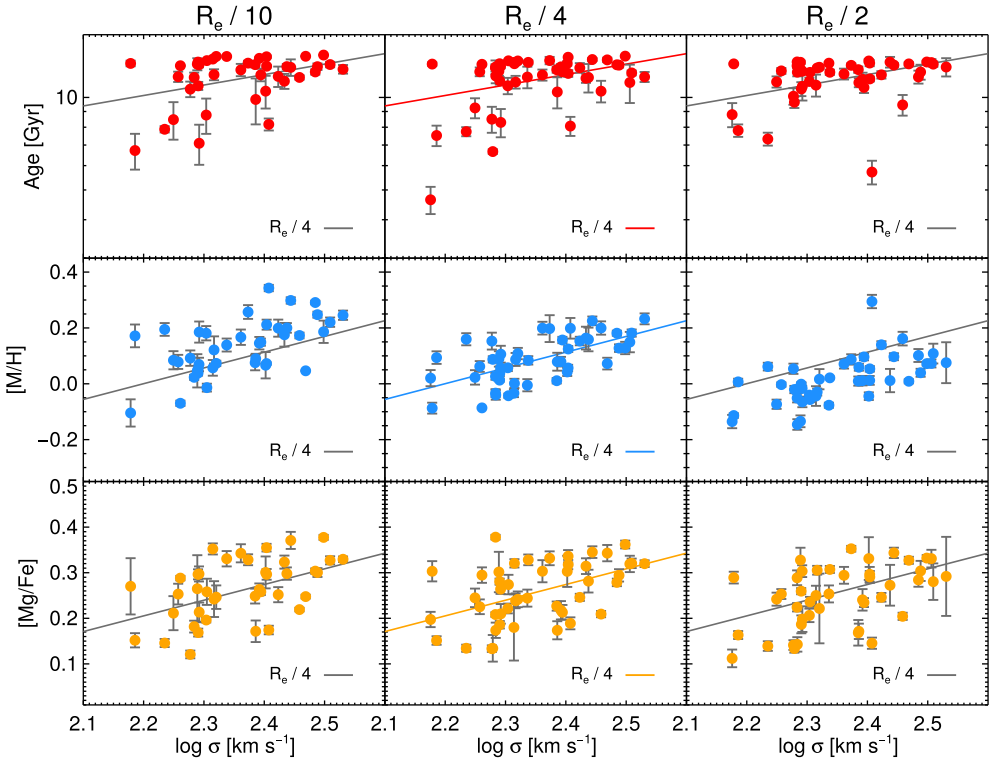

Figure 4. Integrated stellar population trends with velocity dispersion. From left to right, each column corresponds to an integrated measurement over one tenth, one fourth and half R_e, respectively. As a reference, the solid line indicates the best-fitting trend with σ as measured at $R_e/4$. Es become more metal rich and more [Mg/Fe]-enhanced with increasing σ. Our sample of Es exhibits very old ages (red dots), with only a small fraction of younger populations, mostly at low-velocity dispersions. The negative [M/H] gradient at all masses is clear from the second row (blue dots). Orange dots indicate the [Mg/Fe] measurements, which do not show any net radial variation.

5.2 Characteristic gradients

Alternatively, we also analysed the stellar population properties by looking at the average radial age, metallicity, and [Mg/Fe] gradients in different σ bins. Following Fig. 1, we separated our sample into three bins according to the central velocity dispersion, and combined all the measurements to obtain the average radial profiles. These characteristic radial profiles, for a given central velocity dispersion, are shown in Fig. 5. To quantify the differences among them, in

Table 2. Best-fitting stellar population gradients for our three velocity dispersion bins. The age, metallicity, and [Mg/Fe] radial gradients were fitted to a $\alpha + \beta \log R/R_e$ linear relation. We list here the best-fitting coefficients, namely, the stellar population value at the R_e (α), and the logarithmic gradient slope (β).

	Age_{Re} [log Gyr]	∇_{age} [log Gyr/log R]	$[\text{M/H}]_{Re}$ [dex]	$\nabla_{[\text{M/H}]}$ [dex/log R]	$[\text{Mg/Fe}]_{Re}$ [dex]	$\nabla_{[\text{Mg/Fe}]}$ [dex/log R]
$\sigma > 300\,\text{km s}^{-1}$	$1.113^{\pm 0.008}$	$0.013^{\pm 0.006}$	$-0.029^{\pm 0.010}$	$-0.269^{\pm 0.012}$	$0.312^{\pm 0.007}$	$0.001^{\pm 0.009}$
$200 < \sigma < 300\,\text{km s}^{-1}$	$1.087^{\pm 0.004}$	$-0.005^{\pm 0.003}$	$-0.031^{\pm 0.005}$	$-0.187^{\pm 0.007}$	$0.252^{\pm 0.004}$	$-0.024^{\pm 0.006}$
$\sigma < 200\,\text{km s}^{-1}$	$1.020^{\pm 0.005}$	$-0.024^{\pm 0.008}$	$-0.089^{\pm 0.003}$	$-0.158^{\pm 0.006}$	$0.186^{\pm 0.003}$	$-0.047^{\pm 0.006}$

Table 2 we report the (χ^2) best-fitting linear gradients. Note that the fits are based on all individual radial measurements, i.e. using the 2D stellar population maps normalized to the effective radius (see Fig. 3), and not on the average profiles shown in Fig. 5.

Age. The downsizing mentioned in Section 5.1 is also clear from Fig. 5, where low-σ galaxies are younger at all radii than high-σ objects. Interestingly, the small fraction of young populations seen in Fig. 4 is no longer visible in the mean age profile. This shows that the bulk of the stellar mass is dominated by old stars (age >10 Gyr). The slope of the age gradients, although rather small, becomes steeper (i.e. more negative) with decreasing velocity dispersion, suggesting an increasing fraction of younger stellar populations in the outer parts of low-σ Es.

Metallicity. We found that the characteristic metallicity gradients are negative in the velocity dispersion range probed by our sample, with more massive galaxies being more metal rich. However, in contrast to Sánchez-Blázquez et al. (2007) and Kuntschner et al. (2010) (but see also Gorgas, Efstathiou & Aragon Salamanca 1990; Gonzalez & Gorgas 1995; La Barbera et al. 2012), we found that the average metallicity gradient steepens with increasing galaxy stellar velocity dispersion. Hence, galaxies with higher σ are not only more metal rich, but also exhibit more pronounced metallicity gradients. This change in the slope of the metallicity gradient is mostly related to the central regions ($\log R/R_e < -0.5$). Excluding later morphological types (E6 and E7) does not affect the steepening of the metallicity gradients and, thus, confusion between Es and S0s is not likely to drive the $\nabla_{[\text{M/H}]}$ variation.

To assess whether the steepening of the metallicity gradients is an actual feature, or whether it is driven by systematics in the stellar populations analysis, we compared in Fig. 6 the radial variation of the combined index [MgFe52]', as defined in Kuntschner et al. (2010), of our three velocity dispersion bins. This index is almost a pure metallicity indicator, weakly depending on [Mg/Fe], and therefore it is a rather model-independent proxy for metallicity variations. Mimicking the behaviour of metallicity gradients shown in Fig. 5, the radial variation in the [MgFe52]' index gets steeper with increasing velocity dispersion. Using the same linear fitting scheme as above and considering only the central regions ($\log R/R_e < -0.5$), the measured [MgFe52]' gradients equal to $\nabla_{[\text{MgFe52}]'} = -0.21 \pm 0.03$, -0.30 ± 0.02, and -0.37 ± 0.03 for the low-σ, intermediate-σ and high-σ bins, respectively, further supporting that galaxies with higher stellar velocity dispersions exhibit steeper metallicity gradients.

[Mg/Fe]. The rather flat character of the [Mg/Fe] profiles is clearly shown in Fig. 5, and confirmed by the best-fitting gradients listed in Table 2, which suggest a mild trend with σ. Galaxies with higher velocity dispersions have, on average, slightly positive [Mg/Fe] radial gradients, but this mean gradient tends to become more negative for galaxies with lower velocity dispersions. Notice that, at all radii, high-σ galaxies are more [Mg/Fe]-enhanced than low-σ objects.

6 DISCUSSION

We have shown that both the normalization and the slope of the stellar populations gradients in Es depend on the central velocity dispersion. Regarding the age of the stellar populations within our sample, the bulk of stars are old, typically formed $\gtrsim$ 10 Gyr ago. On top of the dominant old stellar component, younger populations can form later due to the either metal-rich, recycled gas expelled by SNe and evolved stars, or accretion of more pristine gas from the intergalactic medium. Although these new generations of stars marginally contribute to the mass budget, their high luminosity explains the diversity of age values shown in Fig. 4. This so-called *frosting* populations were first proposed by Trager et al. (2000b), and have also been invoked to explain the ultraviolet properties of nearby ETGs (Vazdekis et al. 2016).

The averaged age gradients (top panel in Fig. 5) probe the overall formation of Es, minimizing the stochastic frosting effect. The transition from a slightly positive age gradient in massive Es towards slightly negative for lighter objects (see Table 2) is expected according to closed-box ETG formation scenarios (Pipino & Matteucci 2004; Pipino et al. 2006). Due to the continuous gas infall at the formation epoch, star formation lasted longer in the central regions of massive galaxies, leading to the observed positive age gradient in the highest σ bin. As stars and dark matter become less concentrated with decreasing galaxy mass (e.g. Bertin, Ciotti & Del Principe 2002; Ferrarese et al. 2006; Kormendy et al. 2009; van Uitert et al. 2013; Tortora et al. 2014), the efficiency to drive and retain the gas in the centre also decreases, hence, creating flatter or even negative age profiles. This transition in the age gradients, from high- to low-σ galaxies, is in agreement with the gradual dominance of rotationally supported systems among lower-mass ($M \sim 10^{11} \text{M}_\odot$) ETGs (Emsellem et al. 2007, 2011; Cappellari et al. 2013), as well as with implementations of semi-analytical models (Porter et al. 2014; Lacey et al. 2016; Tonini et al. 2017).

As expected from the standard interpretation of the [Mg/Fe] as a star formation timer, we found that average age and [Mg/Fe] radial variations seem to be, at least, partially correlated (see Fig. 5). The marginally positive [Mg/Fe] gradient of our highest σ bin suggests that the star formation lasted longer in the centre than in the outskirts, which is consistent with the age profile. On the other hand, the low [Mg/Fe] values in the outer regions of low-σ galaxies might indicate a more extended star formation, which is consistent with the observed age gradient.

Our measurements favour a gradual steepening of the metallicity gradients with increasing galaxy velocity dispersion. Although studies over wide ranges of masses and morphological types support similar trends (González Delgado et al. 2015), detailed stellar population analysis of ETGs tends to favour the opposite, i.e. galaxies with higher velocity dispersions exhibiting flatter metallicity gradients (Sánchez-Blázquez et al. 2007; Spolaor et al. 2009, 2010; Kuntschner et al. 2010). Theoretically, a monolithic-like formation

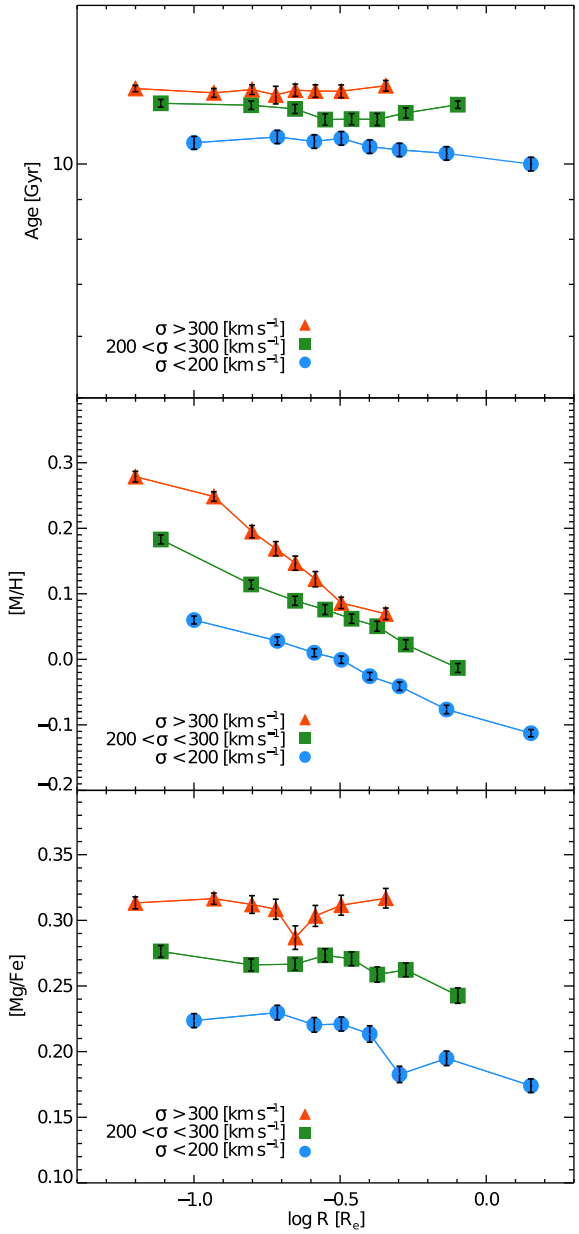

Figure 5. Average stellar population gradients as a function of galaxy velocity dispersion. Each radial profile consists of eight bins, each of them containing the same number of *individual* radial measurements. Error bars indicate the uncertainty on the mean value. The average profile of galaxies with effective velocity dispersions below 200 km s^{-1}is indicated with blue filled circles, green squares correspond to galaxies with $200 < \sigma < 300$ km s^{-1}, and finally the gradients of the most massive galaxies ($\sigma > 300$ km s^{-1}) are shown with red filled triangles. From top to bottom, we show the age, metallicity, and [Mg/Fe] average radial gradients. Age and [Mg/Fe] behave similarly, as galaxies become older and more [Mg/Fe]-enhanced with increasing σ, with rather flat profiles. Galaxies with higher σ are also more metal rich, and the slope of the gradient significantly steepens for galaxies with larger velocity dispersions.

path for ETGs should result in a clear trend between galaxy mass and metallicity gradient slope, as suggested by our measurements, with most massive galaxies hosting steeper metallicity gradients (Chiosi & Carraro 2002; Kawata & Gibson 2003). To what extent this applies to real ETGs, in particular due to the effect of successive mergers (Cook et al. 2016), will be discussed in the next section.

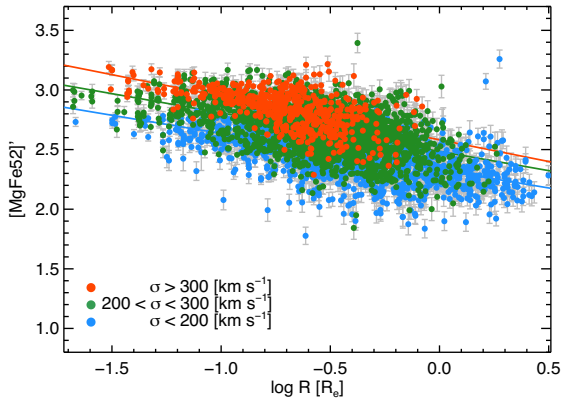

Figure 6. [MgFe52]' index gradients colour-coded as a function of galaxy central velocity dispersion. As in Fig. 5, red, green, and blue filled symbols correspond to individual measurements within galaxies with $\sigma > 300$ km s^{-1}, $200 < \sigma < 300$ km s^{-1}, and $\sigma < 200$ km s^{-1}, respectively. The best-fitting relation for each cloud of points is shown as a solid coloured line. Being independent of any model assumption, the radial trends of this total metallicity-sensitive line-strength support the steepening of the metallicity gradients with increasing velocity dispersion shown in Fig. 5.

6.1 Cosmological evolution of the stellar population gradients

The short formation time-scales (e.g. Thomas et al. 2005), old ages (e.g. Trager et al. 2000a), light profile concentration (e.g. Graham, Trujillo & Caon 2001), and recurrent appearance of old galaxies at high redshifts (Lonoce et al. 2015; Kriek et al. 2016; López-Corredoira et al. 2017) ought to indicate that ETGs were formed very rapidly, in gas-rich, high star formation rate events beyond $z \sim 2$, or even earlier (Wellons et al. 2015). This would imply that the bulk of stars within ETGs were formed in situ, in a monolithic-like fashion, leading to the observed scaling relations between stellar population properties and galaxy mass.

However, in a ΛCDM Universe, galaxies and their dark matter haloes do not evolve in isolation. The role of mergers in shaping the evolution of galaxies is particularly relevant for ETGs, as suggested by the morphology–density relation (Dressler 1980; Postman & Geller 1984; Cappellari et al. 2011), and by the lack of net angular momentum, particularly in high-mass objects (Emsellem et al. 2011; Cappellari et al. 2013; Falcón-Barroso et al. 2017). Furthermore, massive ETGs have grown in size a factor of ∼4 since $z \sim 2$ (e.g. Trujillo et al. 2004, 2007; Daddi et al. 2005; Franx et al. 2008; van Dokkum et al. 2010; van der Wel et al. 2014), presumably through the accretion of less massive satellites (Naab, Johansson & Ostriker 2009; Hopkins et al. 2010; Hilz et al. 2012).

To reconcile monolithic and merger-driven properties of ETGs, a mixed formation path has been proposed and developed over the last years, both theoretically (Oser et al. 2010, 2012; Navarro-González et al. 2013; Shankar et al. 2013) and observationally (Pastorello et al. 2014; Martín-Navarro et al. 2015a; Foster et al. 2016). This so-called two-phase formation scenario can be summarized as follows.

(1) The gas-rich environment at redshift $z \sim 2$–3 favoured the formation of massive, compact and highly star-forming discs, either via violent instabilities (Gammie 2001; Dekel, Sari & Ceverino 2009; Krumholz & Burkert 2010) or through gas-rich mergers (Barnes & Hernquist 1991; Mihos & Hernquist 1996; Hopkins et al. 2006). Note that given their dissipative character, these two mechanisms of gas fuelling towards the centre of galaxies are virtually indistinguishable after they take place. The end products of this first stage are massive, compact, and rotating *blue nuggets*, which ultimately

quench into *red nuggets* (e.g. Barro et al. 2013; Dekel & Burkert 2014; Barro et al. 2017). The stellar population properties of these *red nuggets* should be those expected in a classical monolithic collapse, i.e. steep and negative radial gradients in metallicity, but a radially increasing [Mg/Fe] (Chiosi & Carraro 2002; Kawata & Gibson 2003; Pipino & Matteucci 2004; Pipino et al. 2006). The scaling relations between stellar population properties and galaxy mass get established during this stage.

(2) After the star formation within *red nuggets* is quenched, their later evolution is driven by mergers. In the case of ETGs, these mergers have to be dry, otherwise they would host young stellar populations at $z \sim 0$. However, it is also possible that at least a fraction of *red nuggets* have accreted a significant amount of gas since they were formed, leading to bulge-dominated spiral galaxies (Graham 2013; Graham, Dullo & Savorgnan 2015; de la Rosa et al. 2016). Massive ETGs sometimes exhibit complex internal kinematics, signatures of major (dry) mergers (Bois et al. 2011; Emsellem et al. 2011; Naab et al. 2014). However, since the pristine scaling relations imprinted in phase (1) are conserved, major mergers can not be responsible for the size evolution of ETGs. Thus, dry accretion of low-mass satellites is thought to be the main evolutionary channel for ETGs during this second stage (Naab et al. 2009; Hopkins et al. 2010; Hilz et al. 2012), although additional mechanisms might be required (Yıldırım et al. 2017). This size and mass growth is mostly driven by the accretion of relatively massive satellites, with masses typically between 1:4 and 1:10 that of the central (Bluck et al. 2012; López-Sanjuan et al. 2012; Ferreras et al. 2014). As these minor satellites fall towards the centre of the more massive central ETG, dynamical friction strips apart the stars of the satellites and their stellar mass remains in the outskirts (Lackner et al. 2012). Such dry growth preserves the monolithic-like properties of massive ETGs, but makes them evolve in size.

Therefore, the stellar population properties observed in present-day massive ETGs are expected to be the combination of the in situ formation of the core, plus the *ex situ* (accreted) material from low-mass satellites deposited in the outer regions (e.g. Ciotti, Lanzoni & Volonteri 2007; Oser et al. 2010, 2012; Navarro-González et al. 2013; Hirschmann et al. 2014; Rodriguez-Gomez et al. 2016). Hence, if one wants to safely understand and interpret the stellar population properties at $z \sim 0$, in situ and *ex situ* processes have to be decoupled. Fortunately, since galaxy mergers are a stochastic process, it is possible that a fraction of *red nuggets* have passively evolved since $z \sim 2$ without accreting any *ex situ*-formed material (Quilis & Trujillo 2013; Stringer et al. 2015). Just recently, a sample of galaxies fulfilling all the characteristics to be considered nearby *red nuggets* (or massive relic compact galaxies) has been identified in the local Universe (van den Bosch et al. 2012; Trujillo et al. 2014; Martín-Navarro et al. 2015a; Ferré-Mateu et al. 2017; Yıldırım et al. 2017). These objects offer the unique possibility of studying the baryonic processes that took place in phase (1), minimizing the influence of the accreted material. Moreover, by comparing these massive relic galaxies to those measured in standard $z \sim 0$ Es, we isolate the effects of phase (2) on the stellar population properties.

In Fig. 7 we show the mean age, metallicity, and [Mg/Fe] gradients of Es from the present work, compared to those measured for the massive relic galaxy sample of Yıldırım et al. (2017) with similar stellar velocity dispersion ($\sigma_e \sim 270$ km s^{-1}). To avoid systematics in the stellar population analysis, we repeated the fitting process described in Section 4.1 for the massive relic galaxies, instead of using the values published in Yıldırım et al. (2017).

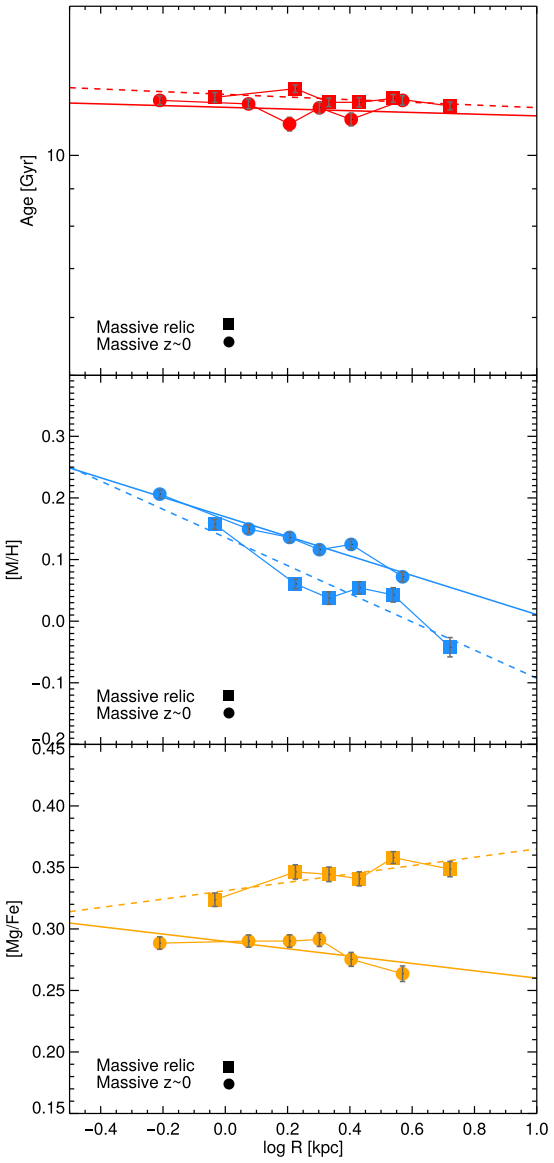

Figure 7. Stellar population gradients of massive relic galaxies. Same as in Fig. 5, but now comparing a sample of nearby relic galaxies (squares) and standard Es of similar masses (circles). Red, blue, and yellow correspond to the age, metallicity, and [Mg/Fe] measurements. In order to account for the size evolution of massive ETGs since $z \sim 2$–3, we plot the stellar population properties as a function of radial distances in units of kpc, rather than R_e. Age profiles are equally flat, but *red nugget* descendants are on average slightly older. On the other hand, the metallicity gradients strongly differ, being flatter in standard nearby Es. The steep metallicity gradient and the increasing [Mg/Fe] with radius are compelling evidence supporting that massive relic galaxies are direct descendants of the high-z population of massive galaxies (*blue/red nuggets*).

The mean age gradients for standard nearby Es and for compact relic galaxies are both rather flat. The main difference among them is that nearby Es are slightly (~ 1 Gyr) younger, which is consistent with a more extended star formation. Although mergers in phase (2) have to be predominantly dry, ETGs are not completely gas-free (Young et al. 2014; Lagos et al. 2014). Thus, a small fraction of merger-induced star formation is expected, in agreement with the age gradients shown in Fig. 7.

On the other hand, radial metallicity gradients in compact relic galaxies are significantly steeper than in standard Es, in remarkable agreement with theoretical predictions (Taylor & Kobayashi 2017). These differences cannot be explained by late star formation, as this would also radially affect the age profile. Alternatively, the flattening of the metallicity gradient is naturally expected if minor mergers actually drive the size growth of ETGs. Basic dynamical arguments indicate that accreted satellites populate the outskirts of the central galaxy, at a distance determined by their mass ratio (Tal & van Dokkum 2011). The more massive a satellite is, the further inside the central galaxy it is deposited. This, combined with the aforementioned mass-dependent contribution to the size growth (López-Sanjuan et al. 2012), implies a differential radial accretion, with the mass growth taking place predominantly in the outskirts of the central galaxy. Note also that the mass–metallicity relation would imply a radial stratification in the metallicity of the accreted material: stars from (massive) metal-rich satellites will populate the inner regions of the central ETGs, which are already more metal rich than the outskirts. The combination of these two processes, differential growth plus metallicity stratification, can explain the observed flattening in the metallicity profiles of nearby Es. This scenario could also explain our finding of a steepening in the metallicity gradients with increasing σ, as well as the differences with respect to previous results. Our gradients, in particular for the high-σ bin, are restricted to the central regions ($R \lesssim 0.5 R_e$), where the signature of a possible monolithic-like collapse is expected to be less affected by mergers, and star formation is also expected to last longer.

Interesting differences are also found in the [Mg/Fe] gradients. In relic compact galaxies, [Mg/Fe] increases with radius, in perfect agreement with monolithic-like formation scenarios (Pipino et al. 2006), further supporting that this kind of objects are the nearby descendant of the high-z *red nuggets*. Over cosmic time, the [Mg/Fe] gradients have experienced a strong variation ($\delta\nabla_{[Mg/Fe]}/\nabla_{[Mg/Fe]} \sim -1.8$), even more important than the change in metallicity ($\delta\nabla_{[M/H]}/\nabla_{[M/H]} \sim -0.5$). Although naively one would expect a similar variation in both quantities, metallicity and [Mg/Fe] values measured in a galaxy are set in different time-scales. Whereas the overall metallicity is rapidly determined by core-collapse SNe, in scales of a few hundred Myr, [Mg/Fe] probes much larger time-scales ($\sim$ Gyr), driven by successive Type Ia SNe explosions (e.g. Vazdekis et al. 1996). Hence, metallicity hardly evolves with time, but [Mg/Fe] does (Feltzing, Holmberg & Hurley 2001; Bensby, Feltzing & Oey 2014; Bergemann et al. 2014). As the size growth of massive ETGs occurs, the stellar populations accreted in their outskirts are more evolved, and presumably they would be less [Mg/Fe]-enhanced. We therefore speculate that the strong variation in the [Mg/Fe] gradient of ETGs, since they were formed as *red nuggets* to what we observe at $z \sim 0$, is due to the late accretion of low-mass satellites with depleted [Mg/Fe]: the later the accretion, the later the satellite quenching, the lower the [Mg/Fe] value of the accreted stars. Metallicity, on the other hand, is rather independent of the satellite accretion time, and therefore its radial gradient shows a weaker variation with redshift.

In Appendix B, we prove that the differences in the radial [Mg/Fe] trends of compact and massive Es are clearly seen at the level of line-strengths (i.e. without relying on stellar population models), hence proving the robustness of our results.

It is worth mentioning that our sample selection, excluding S0 galaxies, provides a cleaner test for the cosmological evolution of the stellar population gradients, as the influence of mergers is likely to be negligible compared to Es (e.g. Cappellari 2016). Moreover, given the high masses of relic compact galaxies, we expect that their $z \sim 0$ descendant will be mostly Es, as the number density of S0 galaxies decreases with increasing galaxy mass. However, absolute measurements of the change in the slope of the stellar population properties need a more complete sample of both nearby Es and massive relic galaxies.

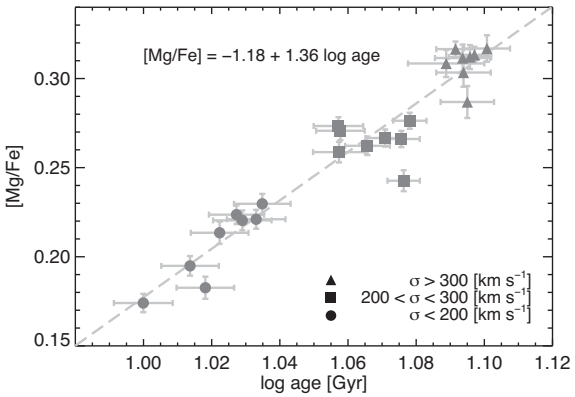

Figure 8. Age–[Mg/Fe] relation for the CALIFA sample. Combination of top and bottom panels of Fig. 5. Filled triangles, squares, and circles correspond to our high-, intermediate-, and low-σ bins. The oldest stellar populations found in the most massive galaxies are more [Mg/Fe]-enhanced than the young populations of low-mass objects. Since both dwarfs and massive galaxies started forming stars at similar times, the age–[Mg/Fe] relation for Es should be interpreted as a consequence of the different formation time-scales: whereas massive galaxies formed their stellar population very rapidly, low-mass objects have experienced more extended star formation histories, leading to lower [Mg/Fe] values and effectively younger ages.

6.2 On the origin of the [Mg/Fe] variations

As described in Section 1, the question of whether the [Mg/Fe] is entirely defined by the formation time-scale of a galaxy or whether it also depends on a variable IMF is still open. In Fig. 8 we show the mean age–[Mg/Fe] relation for the stellar populations in our sample, as derived from the radial measurements shown in Fig. 5. The trend represented in Fig. 8 could be interpreted as the combination of two different phenomena: (1) low-σ galaxies formed their stellar populations later and (2) over more extended periods of time, being therefore younger and less [Mg/Fe]-enhanced. Both properties (young stars plus low [Mg/Fe] ratios) could, in principle, be completely independent. However, very old stars, with ages $\gtrsim$ 12 Gyr, constitute a significant fraction of the stellar mass for all ETG masses, from dwarfs (Koleva et al. 2009; Ryś et al. 2015) to giants (McDermid et al. 2015; de La Rosa et al. 2011). Therefore, the age–[Mg/Fe] relation shown in Fig. 8 seems to be mainly driven by the star formation time-scale, in agreement with the standard interpretation of the [Mg/Fe] ratio. Low-σ galaxies started forming stars at the same time as high-σ ones, but since star formation took longer, they are less [Mg/Fe]-enhanced, and look effectively younger.

However, the analysis of our observations suggests that other mechanisms, in addition to the star formation history, might be needed to explain the abundance pattern of Es. This claim is based on two main results. First of all, age and [Mg/Fe] gradients in massive relic galaxies are anti-correlated (Fig. 7). If the star formation duration was to be the only mechanism driving the abundance pattern in massive ETGs, massive relic galaxies should exhibit a positive radial age variation of $\sim$1.5 Gyr, to be consistent with the

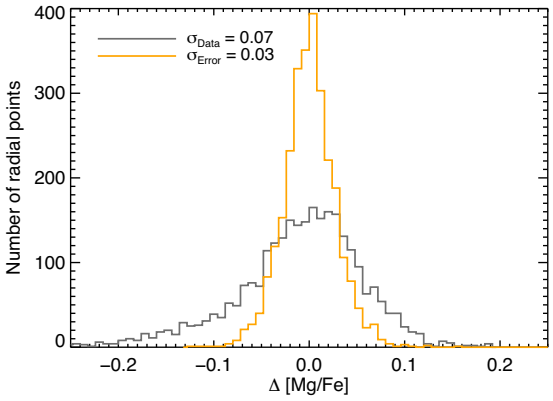

Figure 9. Δ[Mg/Fe] distribution within our sample of CALIFA Es (grey). Δ[Mg/Fe] describes the scatter in the [Mg/Fe] values of stellar populations with a given age. Therefore, in the absence of additional mechanisms other than the duration of the star formation histories, it should be consistent with the observed errors (orange). The notable differences between the two distributions, both in width and in shape, suggest that [Mg/Fe] is not only driven by the star formation time-scale.

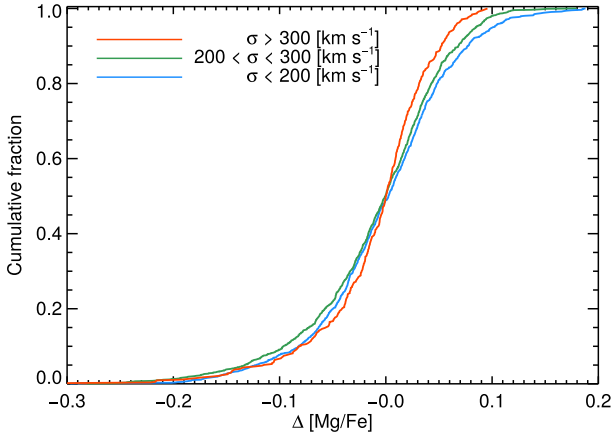

Figure 10. Cumulative distributions of Δ[Mg/Fe] within our three velocity dispersion bins. Galaxies with higher velocity dispersion have a more asymmetrical distribution, with a larger fraction of negative Δ[Mg/Fe] but lower regions where Δ[Mg/Fe] is above the average. This change in the skewness, from $\gamma_1 = -1.31$ for the high-σ bin to $\gamma_1 = -0.42$ for the low-σ one, is compatible with the expected effect of a variable IMF as a function of galaxy mass.

[Mg/Fe] gradient (Fig. 8). Molaeinezhad et al. (2017) have reported a similar decoupling between age and [Mg/Fe] in the bulges of nearby barred galaxies.

The effect of complementary mechanisms can be explored by analysing the [Mg/Fe] distribution at a fixed age. For every spatial bin in our stellar population maps (Fig. 3), we defined the quantity Δ[Mg/Fe] as

$$\Delta[\mathrm{Mg/Fe}] = [\mathrm{Mg/Fe}]_{(x,y)} - \langle[\mathrm{Mg/Fe}]_{\mathrm{age}(x,y)}\rangle,$$

where $[\mathrm{Mg/Fe}]_{(x,y)}$ is the abundance pattern measurement at the (x, y) position, and $\langle[\mathrm{Mg/Fe}]_{\mathrm{age}(x,y)}\rangle$ is the median [Mg/Fe] value of all the points in that galaxy with the same age. Given our limited age resolution,[1] this latter median [Mg/Fe] was evaluated in steps of $\delta\mathrm{age} = 0.5$ Gyr. In practice, Δ[Mg/Fe] defines the scatter in the [Mg/Fe] value for a given age, and its distribution is shown in Fig. 9 combining all galaxies in our sample.

If the only driver of the [Mg/Fe] variations is the duration of the star formation, the distribution of Δ[Mg/Fe] (grey) should be entirely explained by our observational uncertainties (orange). However, it is clear that uncertainties alone do not explain the observed distribution, further suggesting additional mechanisms regulating the [Mg/Fe] enhancement. As discussed in Section 1, IMF variations have been invoked to explain the abundance pattern variations in ETGs. A non-universal IMF is particularly appealing to explain Fig. 9, given the pronounced tail of the Δ[Mg/Fe] distribution towards negative values. The assumption of a bottom-heavier IMF in massive ETGs would reduce the number of massive stars that will end up as core-collapse SNe, leading to lower [Mg/Fe] values than expected assuming a standard IMF slope (Martín-Navarro 2016). Given the IMF slope–σ relation (e.g. Treu et al. 2010; Cappellari et al. 2012; La Barbera et al. 2013), if the IMF is responsible for the asymmetry observed in the [Mg/Fe] distribution, this should be more prominent in our high-σ. In other words, the skewness (γ_1) of the Δ[Mg/Fe] distribution should gradually become more negative when moving from the low-σ to the high-σ bin. The analysis of our data is fully consistent with such a scenario, as γ_1 equals to -0.42, -0.80, and -1.31 in our low-σ, intermediate, and high-σ bins, respectively. The cumulative distribution for the three σ bins is shown in Fig. 10.

Alternatively, it may be possible to explain the Δ[Mg/Fe] tail towards negative values as a consequence of more extended star formation histories. Since our age bins are not infinitively narrow ($\delta\mathrm{age} = 0.5$), there is room for slight differences in star formation time-scales. We have investigated this possibility by comparing the star formation histories in the high and low Δ[Mg/Fe] ends, but no differences were found. In addition, there is no correlation between Δ[Mg/Fe] and age. These results seem to suggest that subtle differences in the star formation history are not likely responsible for the shape of the Δ[Mg/Fe], at least within the level of precision allowed by the data. Whether weaker variations in the star formation at fixed age are important in shaping Δ[Mg/Fe] is yet to be investigated.

It is worth noticing two facts before further interpreting these results. First of all, we have not measured the IMF in our sample of galaxies. Thus, although the quantitative behaviour of Δ[Mg/Fe] agrees with a variable IMF scenario, no conclusive statements can be made. Secondly, the observed trend between IMF slope and galaxy velocity dispersion only applies to the low-mass end of the IMF, i.e. below $M{\sim}1\mathrm{M}_{\odot}$, but not necessarily to the massive stars driving the [Mg/Fe] ratio. Although there is observational evidence of a variable high-mass end IMF slope (Hoversten & Glazebrook 2008; Meurer et al. 2009; Gunawardhana et al. 2011; Nanayakkara et al. 2017), as also supported by the chemical composition of massive ETGs (Vazdekis et al. 1996, 1997; Weidner et al. 2013; Ferreras et al. 2015), results are less conclusive than those focused on the low-mass end.

7 SUMMARY AND CONCLUSIONS

We have analysed a sample of 45 Es drawn from the CALIFA sample, measuring spatially resolved age, metallicity, and [Mg/Fe] maps. We have compared these measurements with a sample of massive relic galaxies. Our findings can be summarized as follows.

[1] For old stellar populations, the age step in BaSTI-based MILES is $\Delta_{\mathrm{age}} = 0.5$ Gyr.

(i) Age and [Mg/Fe] gradients in nearby Es are rather flat, with no strong dependence on galaxy velocity dispersion. However, in contrast with previous studies, we find that the central ($R \lesssim 0.5 R_e$) metallicity gradients become steeper with increasing σ, which could be understood as the imprint of an early monolithic-like formation, preserved in the innermost regions of Es. However, when compared to nearby *red nuggets*, present-day massive Es exhibit flatter metallicity and [Mg/Fe] gradients. We interpret this transition as a combination of the initial monolithic-like, in situ formation at high redshift ($z \gtrsim 2$), plus the later dry accretion of satellites in the outskirts.

(ii) The [Mg/Fe]–age relation observed in all our velocity dispersion bins further supports the classical interpretation of the [Mg/Fe] value as a proxy for the formation time-scales of ETGs. However, additional mechanisms other than the duration of the star formation seem to be required, as age and [Mg/Fe] appear partially anti-correlated at $z \sim 0$. Moreover, there is a significant σ-dependent scatter in [Mg/Fe] at fixed age, not accounted by the observational uncertainties. Variations in the IMF are consistent with our measurements.

Understanding baryonic processes within massive ETGs is particularly challenging due to their old ages and their merger-driven evolutionary paths. However, we have shown here that detailed stellar population analysis and the comparison to nearby massive relic galaxies can be used to reconstruct the star formation processes up to $z \sim 2$. A more complete analysis, considering IMF and elemental abundance variations, as well as deeper observations will bring additional constraints in the future. Moreover, detailed observations of massive quiescence galaxies at higher redshifts will shed light on our results based on nearby objects. These observations will become a reality with the advent of the *James Webb Space Telescope*, combined with ground-based infrared spectrographs such as EMIR (GTC) or MOSFIRE (Keck).

ACKNOWLEDGEMENTS

We would like to thank the referee for a detailed and helpful review of our manuscript. We acknowledge support from grants AYA2016-77237-C3-1-P and AYA2014-56795-P from the Spanish Ministry of Economy and Competitiveness (MINECO), and from SFB 881 The Milky Way System (subproject A7 and A8) funded by the German Research Foundation. IMN acknowledges support from the EU Marie Curie Global Fellowships. GvdV acknowledges funding from the European Research Council (ERC) under the European Union's Horizon 2020 research and innovation programme under grant agreement No 724857 (Consolidator Grant ArcheoDyn).

REFERENCES

Adamek J., Daverio D., Durrer R., Kunz M., 2013, Phys. Rev. D, 88, 103527
Amblard A., Riguccini L., Temi P., Im S., Fanelli M., Serra P., 2014, ApJ, 783, 135
Arrigoni M., Trager S. C., Somerville R. S., Gibson B. K., 2010, MNRAS, 402, 173
Barnes J. E., Hernquist L. E., 1991, ApJ, 370, L65
Barro G. et al., 2013, ApJ, 765, 104
Barro G. et al., 2017, ApJ, 840, 47
Baugh C. M., 2006, Rep. Progress Phys., 69, 3101
Bell E. F., McIntosh D. H., Katz N., Weinberg M. D., 2003, ApJS, 149, 289
Bender R., Burstein D., Faber S. M., 1993, ApJ, 411, 153
Bensby T., Feltzing S., Oey M. S., 2014, A&A, 562, A71
Bergemann M. et al., 2014, A&A, 565, A89
Bernardi M., Sheth R. K., Nichol R. C., Schneider D. P., Brinkmann J., 2005, AJ, 129, 61
Bertin G., Ciotti L., Del Principe M., 2002, A&A, 386, 149
Blakeslee J. P. et al., 2003, ApJ, 596, L143
Bluck A. F. L., Conselice C. J., Buitrago F., Grützbauch R., Hoyos C., Mortlock A., Bauer A. E., 2012, ApJ, 747, 34
Bois M. et al., 2011, MNRAS, 416, 1654
Bond J. R., Kofman L., Pogosyan D., 1996, Nature, 380, 603
Bower R. G., Lucey J. R., Ellis R. S., 1992, MNRAS, 254, 601
Bower R., Schaye J., Frenk C. S., Theuns T., Schaller M., Crain R. A., McAlpine S., 2017, MNRAS, 465, 32
Burstein D., Faber S. M., Gaskell C. M., Krumm N., 1984, ApJ, 287, 586
Cappellari M., 2016, ARA&A, 54, 597
Cappellari M., 2017, MNRAS, 466, 798
Cappellari M., Copin Y., 2003, MNRAS, 342, 345
Cappellari M., Emsellem E., 2004, PASP, 116, 138
Cappellari M. et al., 2011, MNRAS, 416, 1680
Cappellari M. et al., 2012, Nature, 484, 485
Cappellari M. et al., 2013, MNRAS, 432, 1862
Cenarro A. J., Gorgas J., Vazdekis A., Cardiel N., Peletier R. F., 2003, MNRAS, 339, L12
Cervantes J. L., Vazdekis A., 2009, MNRAS, 392, 691
Chiosi C., Carraro G., 2002, MNRAS, 335, 335
Ciotti L., Lanzoni B., Volonteri M., 2007, ApJ, 658, 65
Coelho P., Barbuy B., Meléndez J., Schiavon R. P., Castilho B. V., 2005, A&A, 443, 735
Coelho P., Bruzual G., Charlot S., Weiss A., Barbuy B., Ferguson J. W., 2007, MNRAS, 382, 498
Cole S. et al., 2005, MNRAS, 362, 505
Colless M. et al., 2001, MNRAS, 328, 1039
Conroy C., Graves G. J., van Dokkum P. G., 2014, ApJ, 780, 33
Cook B. A., Conroy C., Pillepich A., Rodriguez-Gomez V., Hernquist L., 2016, ApJ, 833, 158
Daddi E. et al., 2005, ApJ, 626, 680
Davé R., Hernquist L., Katz N., Weinberg D. H., 1999, ApJ, 511, 521
de Bernardis P. et al., 2000, Nature, 404, 955
de La Rosa I. G., La Barbera F., Ferreras I., de Carvalho R. R., 2011, MNRAS, 418, L74
de la Rosa I. G., La Barbera F., Ferreras I., Sánchez Almeida J., Dalla Vecchia C., Martínez-Valpuesta I., Stringer M., 2016, MNRAS, 457, 1916
De Lucia G., Blaizot J., 2007, MNRAS, 375, 2
De Lucia G., Springel V., White S. D. M., Croton D., Kauffmann G., 2006, MNRAS, 366, 499
De Lucia G., Weinmann S., Poggianti B. M., Aragón-Salamanca A., Zaritsky D., 2012, MNRAS, 423, 1277
De Lucia G., Fontanot F., Hirschmann M., 2017, MNRAS, 466, L88
Dekel A., Burkert A., 2014, MNRAS, 438, 1870
Dekel A., Sari R., Ceverino D., 2009, ApJ, 703, 785
Di Matteo T., Springel V., Hernquist L., 2005, Nature, 433, 604
Dressler A., 1980, ApJ, 236, 351
Ellis R. S., Smail I., Dressler A., Couch W. J., Oemler A., Jr, Butcher H., Sharples R. M., 1997, ApJ, 483, 582
Emsellem E. et al., 2007, MNRAS, 379, 401
Emsellem E. et al., 2011, MNRAS, 414, 888
Faber S. M., 1973, ApJ, 179, 731
Falcón-Barroso J. et al., 2011a, MNRAS, 417, 1787
Falcón-Barroso J., Sánchez-Blázquez P., Vazdekis A., Ricciardelli E., Cardiel N., Cenarro A. J., Gorgas J., Peletier R. F., 2011b, A&A, 532, A95
Falcón-Barroso J. et al., 2017, A&A, 597, A48
Feltzing S., Holmberg J., Hurley J. R., 2001, A&A, 377, 911
Ferrarese L. et al., 2006, ApJS, 164, 334
Ferré-Mateu A., Trujillo I., Martín-Navarro I., Vazdekis A., Mezcua M., Balcells M., Domínguez L., 2017, MNRAS, 467, 1929
Ferreras I., La Barbera F., de la Rosa I. G., Vazdekis A., de Carvalho R. R., Falcón-Barroso J., Ricciardelli E., 2013, MNRAS, 429, L15
Ferreras I. et al., 2014, MNRAS, 444, 906
Ferreras I., Weidner C., Vazdekis A., La Barbera F., 2015, MNRAS, 448, L82

Fontanot F., De Lucia G., Hirschmann M., Bruzual G., Charlot S., Zibetti S., 2017, MNRAS, 464, 3812
Foreman-Mackey D., Hogg D. W., Lang D., Goodman J., 2013, PASP, 125, 306
Foster C. et al., 2016, MNRAS, 457, 147
Franx M., van Dokkum P. G., Förster Schreiber N. M., Wuyts S., Labbé I., Toft S., 2008, ApJ, 688, 770
Frenk C. S., White S. D. M., Davis M., Efstathiou G., 1988, ApJ, 327, 507
Gallazzi A., Charlot S., Brinchmann J., White S. D. M., Tremonti C. A., 2005, MNRAS, 362, 41
Gallazzi A., Charlot S., Brinchmann J., White S. D. M., 2006, MNRAS, 370, 1106
Gammie C. F., 2001, ApJ, 553, 174
Gargiulo I. D. et al., 2015, MNRAS, 446, 3820
Geller M. J., Huchra J. P., 1989, Science, 246, 897
González Delgado R. M. et al., 2015, A&A, 581, A103
Gonzalez J. J., Gorgas J., 1995, in Buzzoni A., Renzini A., Serrano A., eds, ASP Conf. Ser. Vol. 86, Fresh Views of Elliptical Galaxies. Astron. Soc. Pac., San Francisco, p. 225 (astro-ph/9507042)
Gorgas J., Efstathiou G., Aragon Salamanca A., 1990, MNRAS, 245, 217
Graham A. W., 2013, in Oswalt T. D., Keel W. C., eds, Planets, Stars and Stellar Systems, Vol. 6. Springer Science+Business Media. Dordrecht, p. 91
Graham A. W., Trujillo I., Caon N., 2001, AJ, 122, 1707
Graham A. W., Dullo B. T., Savorgnan G. A. D., 2015, ApJ, 804, 32
Graves G. J., Faber S. M., Schiavon R. P., 2009a, ApJ, 693, 486
Graves G. J., Faber S. M., Schiavon R. P., 2009b, ApJ, 698, 1590
Greene J. E., Janish R., Ma C.-P., McConnell N. J., Blakeslee J. P., Thomas J., Murphy J. D., 2015, ApJ, 807, 11
Gunawardhana M. L. P. et al., 2011, MNRAS, 415, 1647
Guo Q. et al., 2016, MNRAS, 461, 3457
Hernquist L., Katz N., Weinberg D. H., Miralda-Escudé J., 1996, ApJ, 457, L51
Hilz M., Naab T., Ostriker J. P., Thomas J., Burkert A., Jesseit R., 2012, MNRAS, 425, 3119
Hinshaw G. et al., 2013, ApJS, 208, 19
Hirschmann M., De Lucia G., Wilman D., Weinmann S., Iovino A., Cucciati O., Zibetti S., Villalobos Á., 2014, MNRAS, 444, 2938
Hopkins P. F., Hernquist L., Cox T. J., Di Matteo T., Robertson B., Springel V., 2006, ApJS, 163, 1
Hopkins P. F., Bundy K., Hernquist L., Wuyts S., Cox T. J., 2010, MNRAS, 401, 1099
Hoversten E. A., Glazebrook K., 2008, ApJ, 675, 163
Kauffmann G., White S. D. M., Guiderdoni B., 1993, MNRAS, 264, 201
Kawata D., Gibson B. K., 2003, MNRAS, 340, 908
Keller B. W., Wadsley J., Couchman H. M. P., 2016, MNRAS, 463, 1431
Kelz A. et al., 2006, PASP, 118, 129
Kleineberg K., Sánchez-Blázquez P., Vazdekis A., 2011, ApJ, 732, L33
Koleva M., de Rijcke S., Prugniel P., Zeilinger W. W., Michielsen D., 2009, MNRAS, 396, 2133
Kormendy J., Fisher D. B., Cornell M. E., Bender R., 2009, ApJS, 182, 216
Kriek M. et al., 2016, Nature, 540, 248
Kroupa P., 2001, MNRAS, 322, 231
Kroupa P., 2002, Science, 295, 82
Krumholz M., Burkert A., 2010, ApJ, 724, 895
Kuntschner H. et al., 2010, MNRAS, 408, 97
La Barbera F., Ferreras I., de Carvalho R. R., Bruzual G., Charlot S., Pasquali A., Merlin E., 2012, MNRAS, 426, 2300
La Barbera F., Ferreras I., Vazdekis A., de la Rosa I. G., de Carvalho R. R., Trevisan M., Falcón-Barroso J., Ricciardelli E., 2013, MNRAS, 433, 3017
La Barbera F., Vazdekis A., Ferreras I., Pasquali A., Allende Prieto C., Röck B., Aguado D. S., Peletier R. F., 2017, MNRAS, 464, 3597
Lacey C. G. et al., 2016, MNRAS, 462, 3854
Lackner C. N., Cen R., Ostriker J. P., Joung M. R., 2012, MNRAS, 425, 641
Lagos C. d. P., Davis T. A., Lacey C. G., Zwaan M. A., Baugh C. M., Gonzalez-Perez V., Padilla N. D., 2014, MNRAS, 443, 1002
Lonoce I. et al., 2015, MNRAS, 454, 3912
López-Corredoira M., Vazdekis A., Gutiérrez C. M., Castro-Rodríguez N., 2017, A&A, 600, A91
López-Sanjuan C. et al., 2012, A&A, 548, A7
McDermid R. M. et al., 2015, MNRAS, 448, 3484
Martín-Navarro I., 2016, MNRAS, 456, L104
Martín-Navarro I., La Barbera F., Vazdekis A., Ferré-Mateu A., Trujillo I., Beasley M. A., 2015a, MNRAS, 451, 1081
Martín-Navarro I. et al., 2015b, ApJ, 806, L31
Martín-Navarro I., Brodie J. P., van den Bosch R. C. E., Romanowsky A. J., Forbes D. A., 2016, ApJ, 832, L11
Mehlert D., Thomas D., Saglia R. P., Bender R., Wegner G., 2003, A&A, 407, 423
Meurer G. R. et al., 2009, ApJ, 695, 765
Mihos J. C., Hernquist L., 1996, ApJ, 464, 641
Milone A. D. C., Sansom A. E., Sánchez-Blázquez P., 2011, MNRAS, 414, 1227
Molaeinezhad A., Falcón-Barroso J., Martínez-Valpuesta I., Khosroshahi H. G., Vazdekis A., La Barbera F., Peletier R. F., Balcells M., 2017, MNRAS, 467, 353
Naab T., Johansson P. H., Ostriker J. P., 2009, ApJ, 699, L178
Naab T. et al., 2014, MNRAS, 444, 3357
Nanayakkara T. et al., 2017, MNRAS, 468, 3071
Navarro-González J., Ricciardelli E., Quilis V., Vazdekis A., 2013, MNRAS, 436, 3507
Oser L., Ostriker J. P., Naab T., Johansson P. H., Burkert A., 2010, ApJ, 725, 2312
Oser L., Naab T., Ostriker J. P., Johansson P. H., 2012, ApJ, 744, 63
Pastorello N., Forbes D. A., Foster C., Brodie J. P., Usher C., Romanowsky A. J., Strader J., Arnold J. A., 2014, MNRAS, 442, 1003
Peletier R. F., 1989, PhD thesis,, University of Groningen
Peletier R. F., Vazdekis A., Arribas S., del Burgo C., García-Lorenzo B., Gutiérrez C., Mediavilla E., Prada F., 1999, MNRAS, 310, 863
Pietrinferni A., Cassisi S., Salaris M., Castelli F., 2004, ApJ, 612, 168
Pietrinferni A., Cassisi S., Salaris M., Castelli F., 2006, ApJ, 642, 797
Pipino A., Matteucci F., 2004, MNRAS, 347, 968
Pipino A., Matteucci F., Chiappini C., 2006, ApJ, 638, 739
Planck Collaboration XVI, 2014, A&A, 571, A16
Porter L. A., Somerville R. S., Primack J. R., Johansson P. H., 2014, MNRAS, 444, 942
Postman M., Geller M. J., 1984, ApJ, 281, 95
Quilis V., Trujillo I., 2013, ApJ, 773, L8
Rees M. J., Ostriker J. P., 1977, MNRAS, 179, 541
Rodriguez-Gomez V. et al., 2016, MNRAS, 458, 2371
Roth M. M. et al., 2005, PASP, 117, 620
Ryś A., Koleva M., Falcón-Barroso J., Vazdekis A., Lisker T., Peletier R., van de Ven G., 2015, MNRAS, 452, 1888
Sánchez S. F. et al., 2012, A&A, 538, A8
Sánchez S. F. et al., 2016, A&A, 594, A36
Sánchez-Blázquez P. et al., 2006, MNRAS, 371, 703
Sánchez-Blázquez P., Forbes D. A., Strader J., Brodie J., Proctor R., 2007, MNRAS, 377, 759
Sarzi M. et al., 2006, MNRAS, 366, 1151
Sarzi M. et al., 2010, MNRAS, 402, 2187
Sarzi M. et al., 2013, MNRAS, 432, 1845
Schawinski K., Thomas D., Sarzi M., Maraston C., Kaviraj S., Joo S.-J., Yi S. K., Silk J., 2007, MNRAS, 382, 1415
Schaye J. et al., 2015, MNRAS, 446, 521
Segers M. C., Schaye J., Bower R. G., Crain R. A., Schaller M., Theuns T., 2016, MNRAS, 461, L102
Shankar F., Marulli F., Bernardi M., Mei S., Meert A., Vikram V., 2013, MNRAS, 428, 109
Somerville R. S., Primack J. R., 1999, MNRAS, 310, 1087
Spiniello C., Trager S. C., Koopmans L. V. E., Chen Y. P., 2012, ApJ, 753, L32
Spiniello C., Trager S., Koopmans L. V. E., Conroy C., 2014, MNRAS, 438, 1483
Spolaor M., Proctor R. N., Forbes D. A., Couch W. J., 2009, ApJ, 691, L138

Spolaor M., Kobayashi C., Forbes D. A., Couch W. J., Hau G. K. T., 2010, MNRAS, 408, 272
Springel V. et al., 2005, Nature, 435, 629
Springel V., Frenk C. S., White S. D. M., 2006, Nature, 440, 1137
Stringer M., Trujillo I., Dalla Vecchia C., Martinez-Valpuesta I., 2015, MNRAS, 449, 2396
Tal T., van Dokkum P. G., 2011, ApJ, 731, 89
Taylor P., Kobayashi C., 2017, MNRAS, 471, 3856
Temi P., Brighenti F., Mathews W. G., 2009, ApJ, 695, 1
Terrazas B. A., Bell E. F., Henriques B. M. B., White S. D. M., Cattaneo A., Woo J., 2016, ApJ, 830, L12
Thomas D., Greggio L., Bender R., 1999, MNRAS, 302, 537
Thomas D., Maraston C., Bender R., Mendes de Oliveira C., 2005, ApJ, 621, 673
Thomas J. et al., 2011, MNRAS, 415, 545
Tinsley B. M., 1979, ApJ, 229, 1046
Tonini C., Mutch S. J., Wyithe J. S. B., Croton D. J., 2017, MNRAS, 465, 4133
Tortora C., La Barbera F., Napolitano N. R., Romanowsky A. J., Ferreras I., de Carvalho R. R., 2014, MNRAS, 445, 115
Trager S. C., Faber S. M., Worthey G., González J. J., 2000a, AJ, 119, 1645
Trager S. C., Faber S. M., Worthey G., González J. J., 2000b, AJ, 120, 165
Treu T., Auger M. W., Koopmans L. V. E., Gavazzi R., Marshall P. J., Bolton A. S., 2010, ApJ, 709, 1195
Trujillo I. et al., 2004, ApJ, 604, 521
Trujillo I., Conselice C. J., Bundy K., Cooper M. C., Eisenhardt P., Ellis R. S., 2007, MNRAS, 382, 109
Trujillo I., Ferré-Mateu A., Balcells M., Vazdekis A., Sánchez-Blázquez P., 2014, ApJ, 780, L20
Valdes F., Gupta R., Rose J. A., Singh H. P., Bell D. J., 2004, ApJS, 152, 251
van den Bosch R. C. E., Gebhardt K., Gültekin K., van de Ven G., van der Wel A., Walsh J. L., 2012, Nature, 491, 729
van der Wel A. et al., 2014, ApJ, 788, 28
van Dokkum P. G., 2008, ApJ, 674, 29
van Dokkum P. G., Conroy C., 2010, Nature, 468, 940
van Dokkum P. G., Franx M., 2001, ApJ, 553, 90
van Dokkum P. G., Franx M., Fabricant D., Illingworth G. D., Kelson D. D., 2000, ApJ, 541, 95
van Dokkum P. G. et al., 2010, ApJ, 709, 1018
van Uitert E., Hoekstra H., Franx M., Gilbank D. G., Gladders M. D., Yee H. K. C., 2013, A&A, 549, A7
Vazdekis A., Casuso E., Peletier R. F., Beckman J. E., 1996, ApJS, 106, 307
Vazdekis A., Peletier R. F., Beckman J. E., Casuso E., 1997, ApJS, 111, 203
Vazdekis A., Trujillo I., Yamada Y., 2004, ApJ, 601, L33
Vazdekis A., Sánchez-Blázquez P., Falcón-Barroso J., Cenarro A. J., Beasley M. A., Cardiel N., Gorgas J., Peletier R. F., 2010, MNRAS, 404, 1639
Vazdekis A. et al., 2015, MNRAS, 449, 1177
Vazdekis A., Koleva M., Ricciardelli E., Röck B., Falcón-Barroso J., 2016, MNRAS, 463, 3409
Verheijen M. A. W., Bershady M. A., Andersen D. R., Swaters R. A., Westfall K., Kelz A., Roth M. M., 2004, Astron. Nachr., 325, 151
Vogelsberger M. et al., 2014, MNRAS, 444, 1518
Walcher C. J. et al., 2014, A&A, 569, A1
Walcher C. J., Coelho P. R. T., Gallazzi A., Bruzual G., Charlot S., Chiappini C., 2015, A&A, 582, A46
Wang F. Y., Dai Z. G., 2011, ApJ, 727, L34
Weidner C., Ferreras I., Vazdekis A., La Barbera F., 2013, MNRAS, 435, 2274
Wellons S. et al., 2015, MNRAS, 449, 361
White S. D. M., 1976, MNRAS, 177, 717
White S. D. M., Frenk C. S., 1991, ApJ, 379, 52
Worthey G., Faber S. M., Gonzalez J. J., 1992, ApJ, 398, 69
Worthey G., Faber S. M., Gonzalez J. J., Burstein D., 1994, ApJS, 94, 687
Yamada Y., Arimoto N., Vazdekis A., Peletier R. F., 2006, ApJ, 637, 200
Yıldırım A., van den Bosch R. C. E., van de Ven G., Martín-Navarro I., Walsh J. L., Husemann B., Gültekin K., Gebhardt K., 2017, MNRAS, 468, 4216
Young L. M. et al., 2014, MNRAS, 444, 3408

APPENDIX A: DATA SYSTEMATIC

A clear systematic residual appears at a rest-frame wavelength $\lambda \sim 5640$ Å, as shown in Fig. A1. Although it is negligible in the central parts of the CALIFA field of view, this systematic made impossible a reliable measurement of the affected line-strength indices. Hence, we applied a redshift cut, so we only studied galaxies with $z < 0.026$, which allowed a clean and homogeneous stellar population analysis using the Fe 4383, Hβ_o, Fe 5015, Mgb, and Fe 5270 indices.

APPENDIX B: MODEL-INDEPENDENT ASSESSMENT OF THE [MG/FE] GRADIENTS

As described above, the change in the slope of the [Mg/Fe] gradients from high-z relics to nearby Es is also supported by the Mgb-Fe 5270 index–index diagram shown in Fig. B1, where all the data points

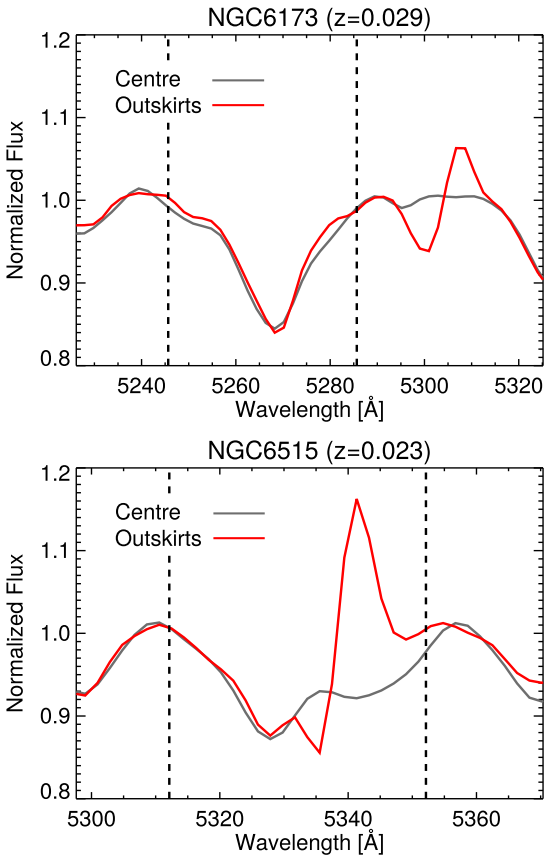

Figure A1. Systematic residual at rest-frame $\lambda \sim 5640$ Å. Grey line shows the central spectrum of the galaxy, whereas the red line corresponds to a radial aperture in the outskirts. The top panel shows the spectral region around the Fe 5270 absorption feature (vertical dashed lines). For NGC 6173, at redshift $z = 0.029$, the systematic affects the red pseudo-continuum of the Fe 5270 line index. The bottom panel shows Fe 5335 spectral feature for NGC 6515 ($z = 0.023$). In this case, the systematic lies over the index central band-pass (vertical dashed lines). To avoid contamination from this systematic, we imposed a hard redshift cut to our sample of galaxies (see details in Section 4.1).

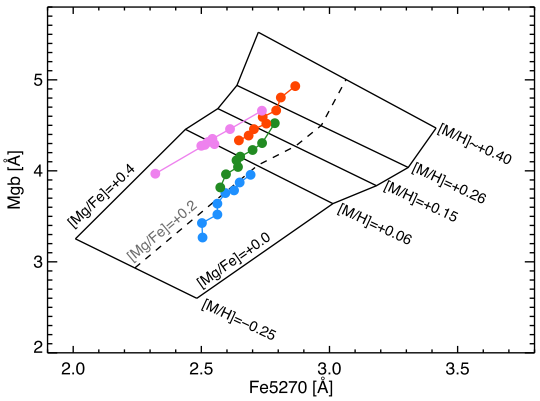

Figure B1. Mg*b*-Fe 5270 index–index diagram. Red, green, and blue filled circles correspond to galaxies with $\sigma > 300\,\mathrm{km\ s^{-1}}$, $200 < \sigma < 300\,\mathrm{km\ s^{-1}}$, and $\sigma < 200\,\mathrm{km\ s^{-1}}$, respectively. For comparison, purple filled circles correspond to the sample of massive relic galaxies. Each symbol indicates a different radial bin, from the centre (highest Mg*b* value) to the outer parts (lowest Mg*b* value), and are shown at a common velocity dispersion of $\sigma = 200\,\mathrm{km\ s^{-1}}$. Radial distances are the same as in Figs 5 and 7. The slope of the Mg*b*-Fe 5270 tracks is clearly different when comparing nearby standard Es and high-z relics, pointing towards a much more pronounced (and positive) [Mg/Fe] gradient for the compact relic galaxies.

have been corrected to a common velocity dispersion of $\sigma = 200\,\mathrm{km\ s^{-1}}$. Explicitly, the corrected index value is given by

$$I_{\mathrm{cor}} = I_{\mathrm{obs}} \frac{M_{x,\sigma=200}}{M_{x,\sigma_{\mathrm{obs}}}}, \tag{B1}$$

where I_{obs} is the observed index value. $M_{x,\,\sigma\,=\,200}$ and $M_{x,\sigma_{\mathrm{obs}}}$ are the line-strength predictions given the best-fitting stellar population parameters $x = \{\mathrm{age,[M/H],[Mg/Fe]}\}$, at the reference ($\sigma = 200\mathrm{km\ s^{-1}}$) and observed ($\sigma_{\mathrm{obs}}$) resolutions, respectively.

The difference response of Mg*b* and Fe 5270 features to total metallicity and [Mg/Fe] allows a model-independent assessment of [M/H] and [Mg/Fe] variations. Radial measurements in nearby Es roughly scatter along constant [Mg/Fe] lines. In contrast, the slope Mg*b*-Fe 5270 track of massive relic galaxies clearly evolve from metal-rich and moderately [Mg/Fe]-enhanced in the centre towards metal-poor (sub-solar) and highly [Mg/Fe] enhancement stellar populations in their outskirts. Although our fitting process included more line-strength indices (see Section 4.1), and therefore it should be interpreted in a relative way, differences in the radial [Mg/Fe] variation appear clearly even at the level of line-strength values.

APPENDIX C: KINEMATICS AND STELLAR POPULATION MAPS

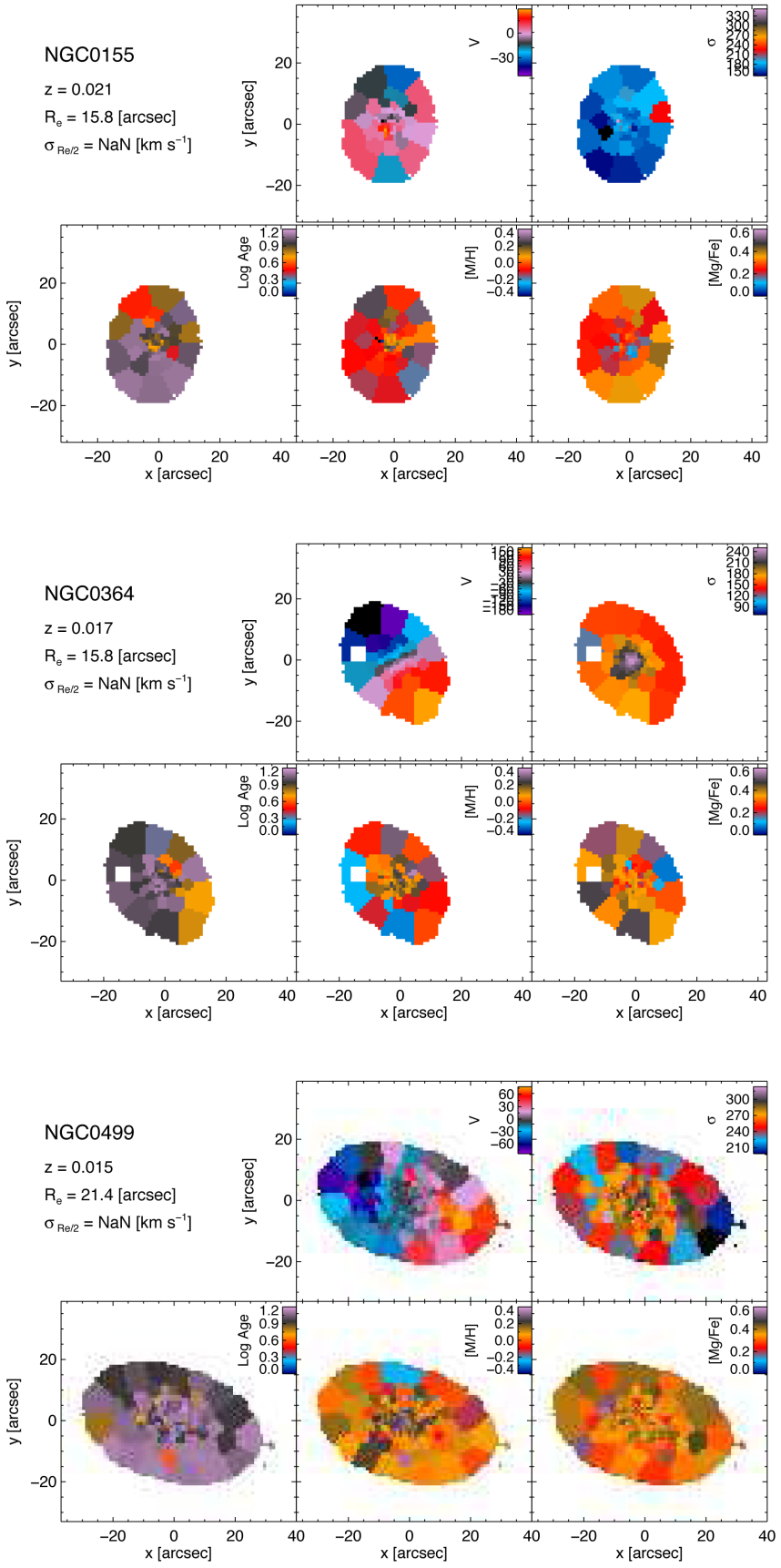

Figure C1. Kinematical and stellar population parameter maps for the CALIFA sample.

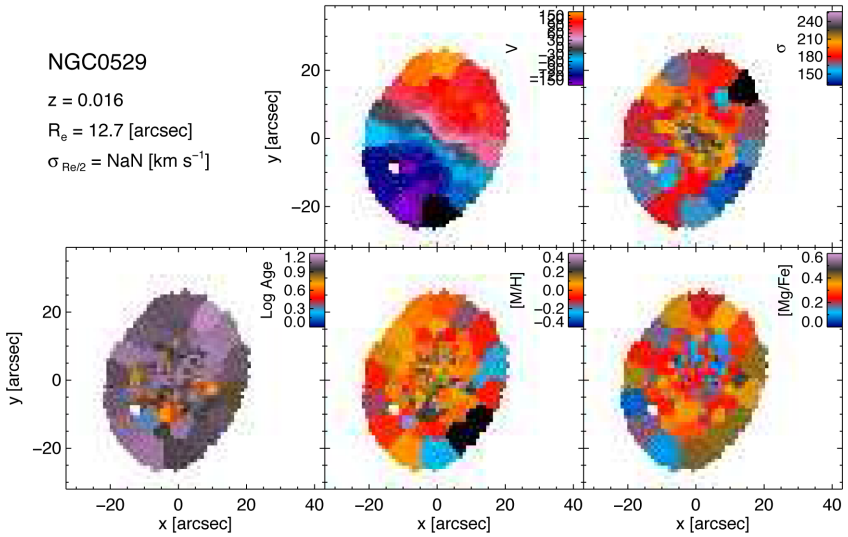

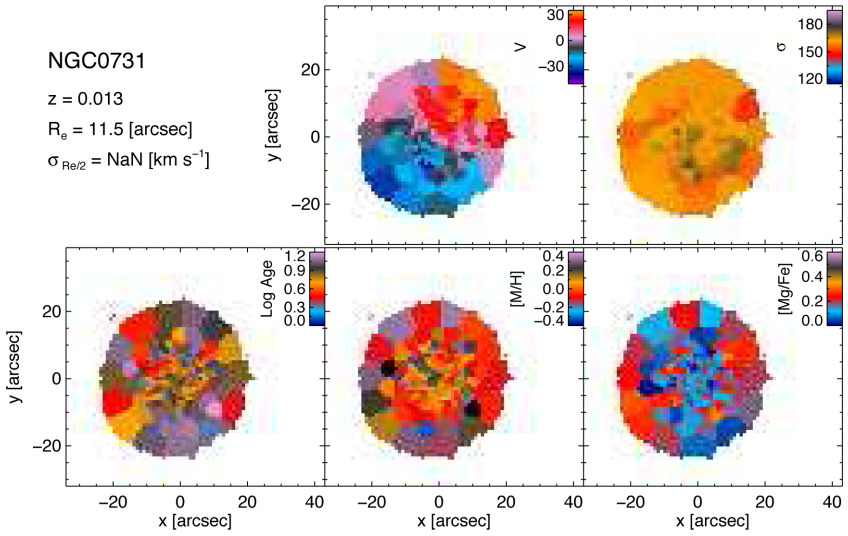

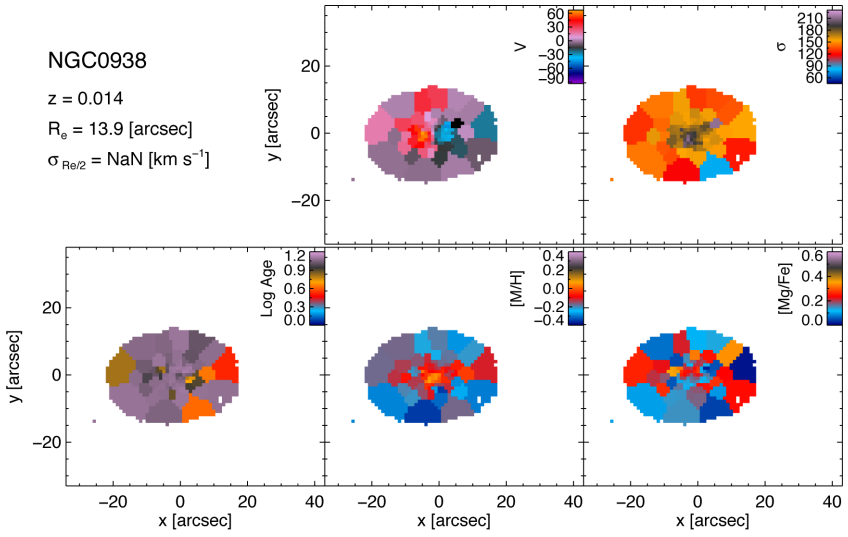

Figure C1 – *continued*

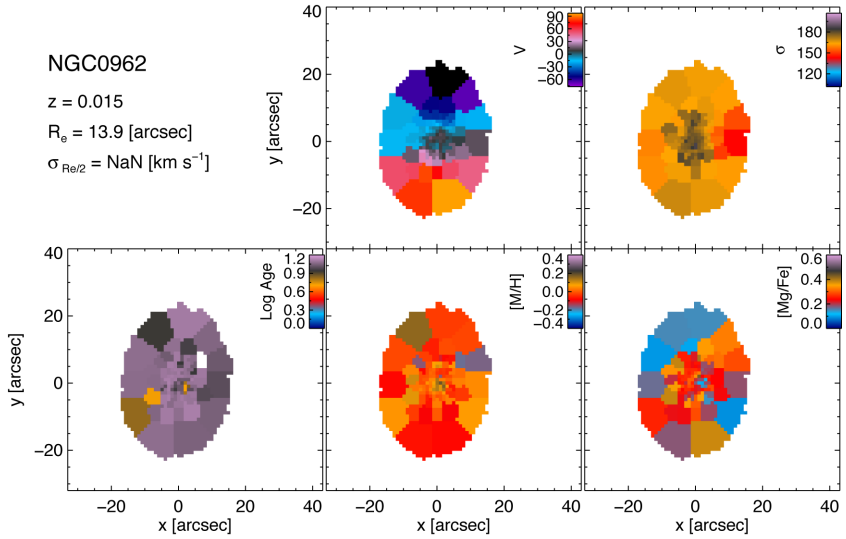

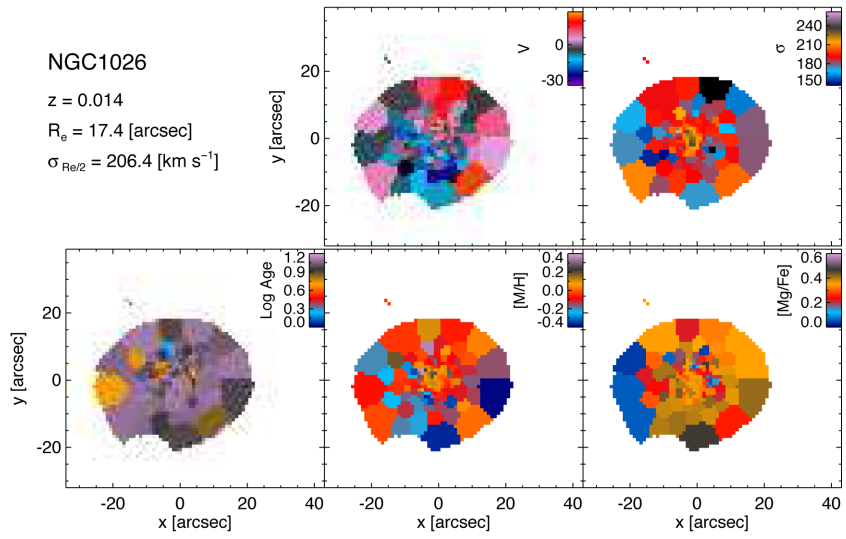

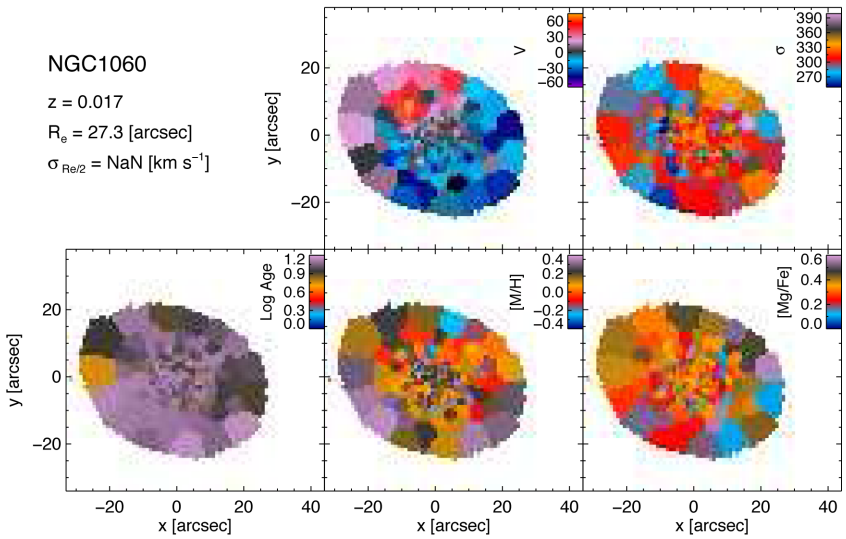

Figure C1 – *continued*

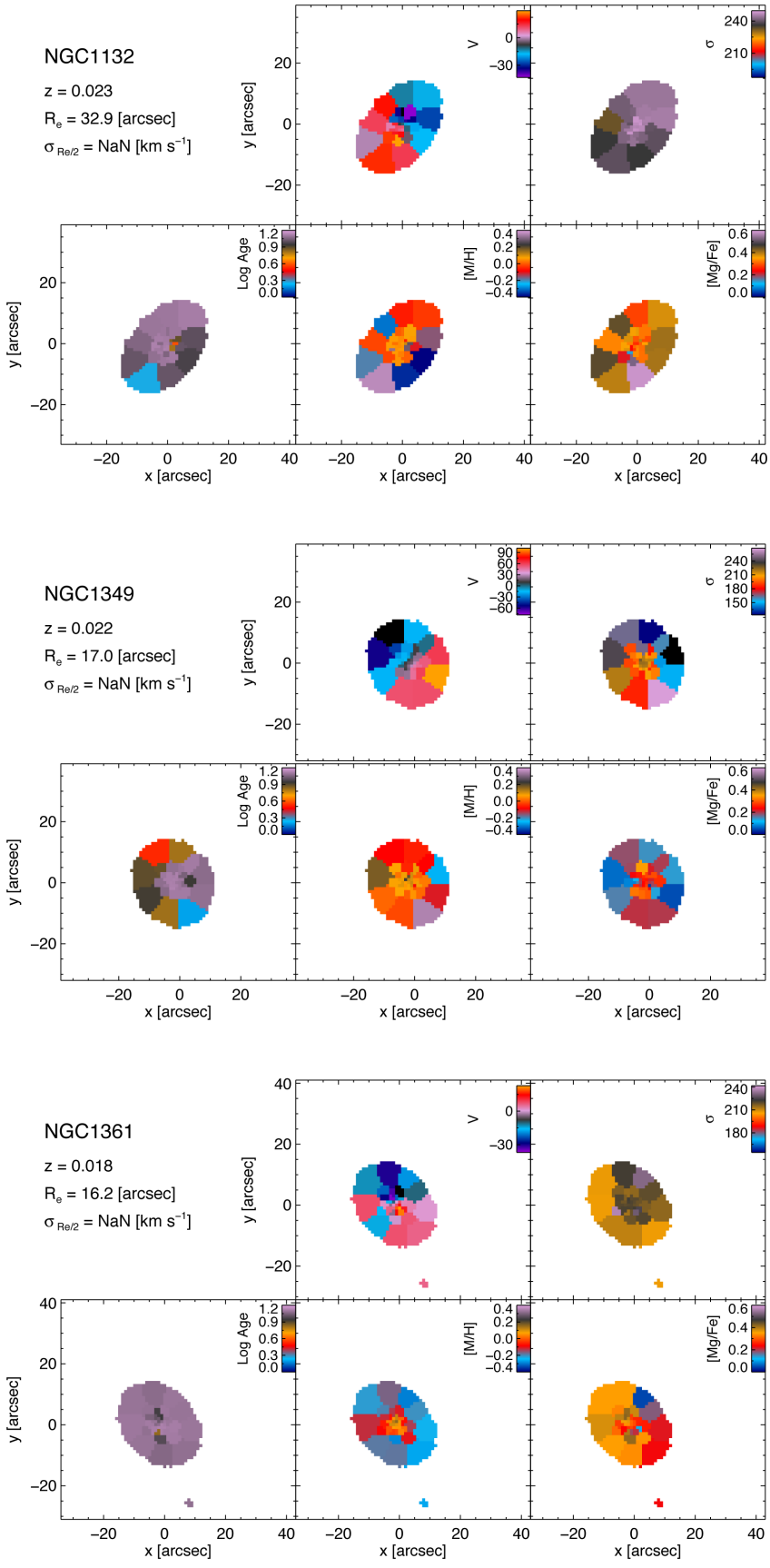

Figure C1 – *continued*

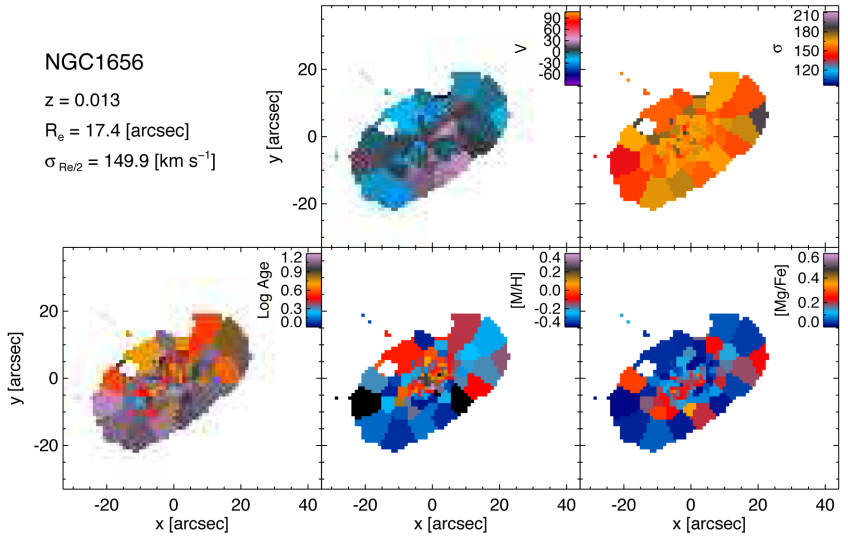

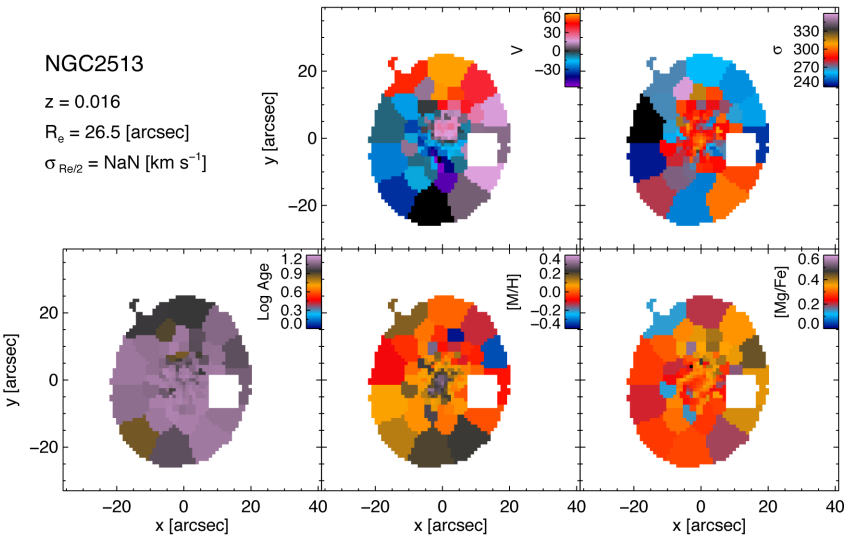

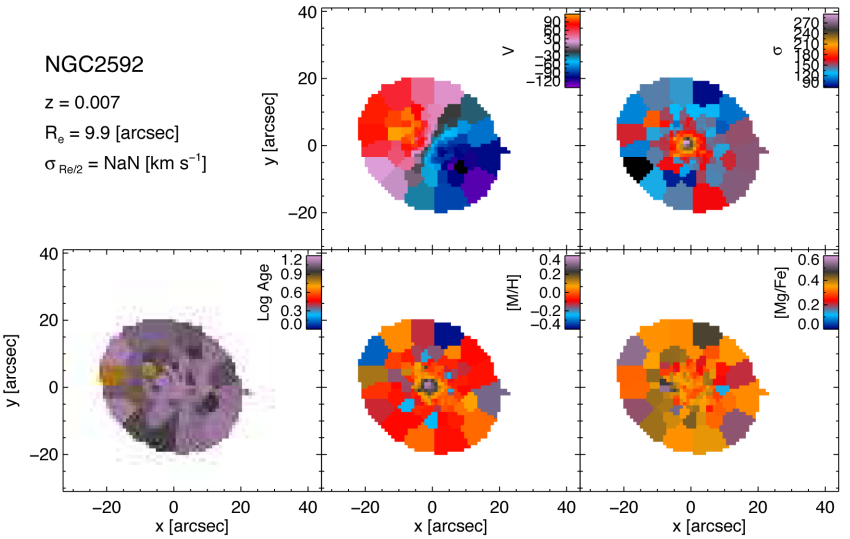

Figure C1 – *continued*

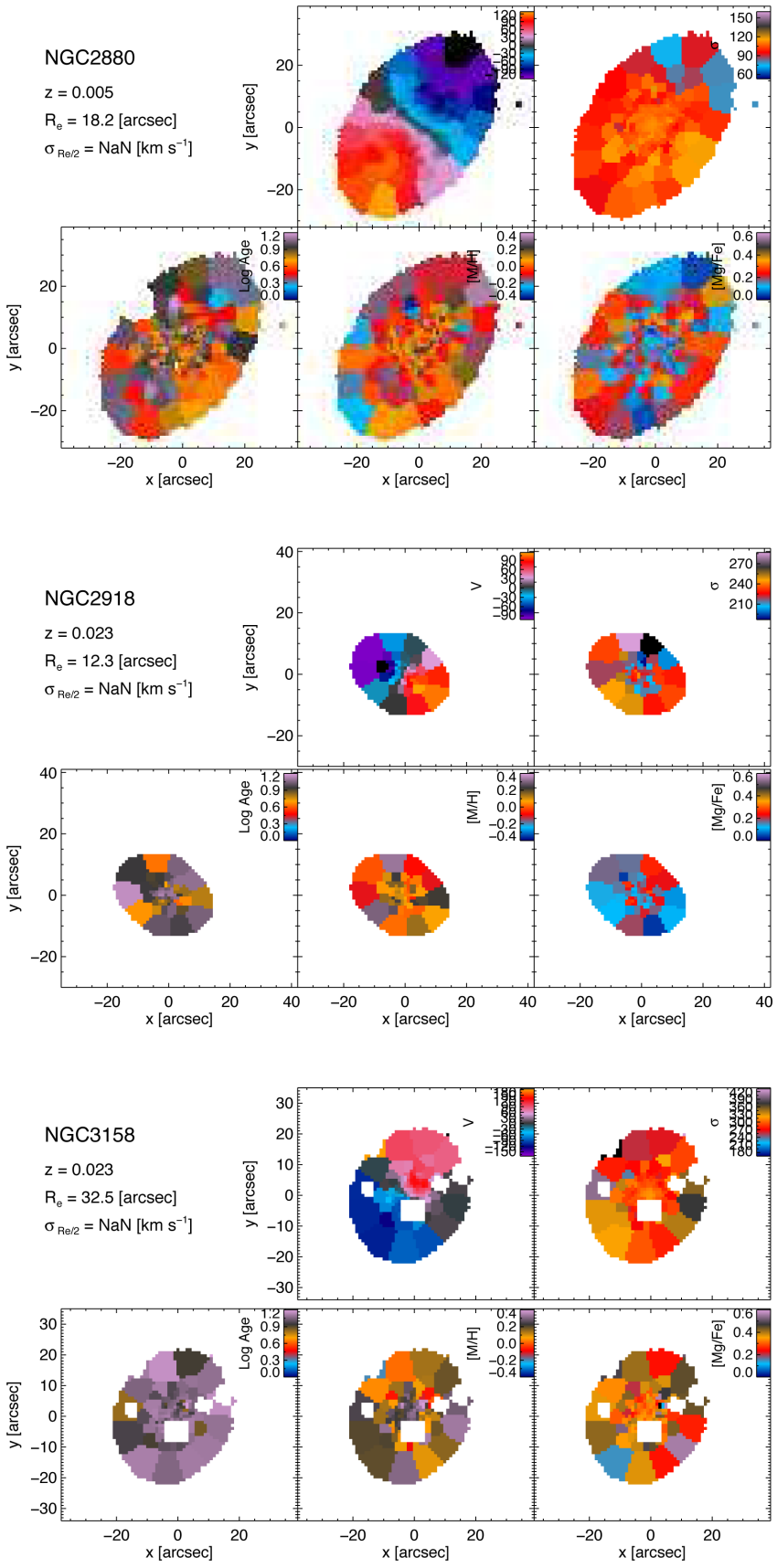

Figure C1 – *continued*

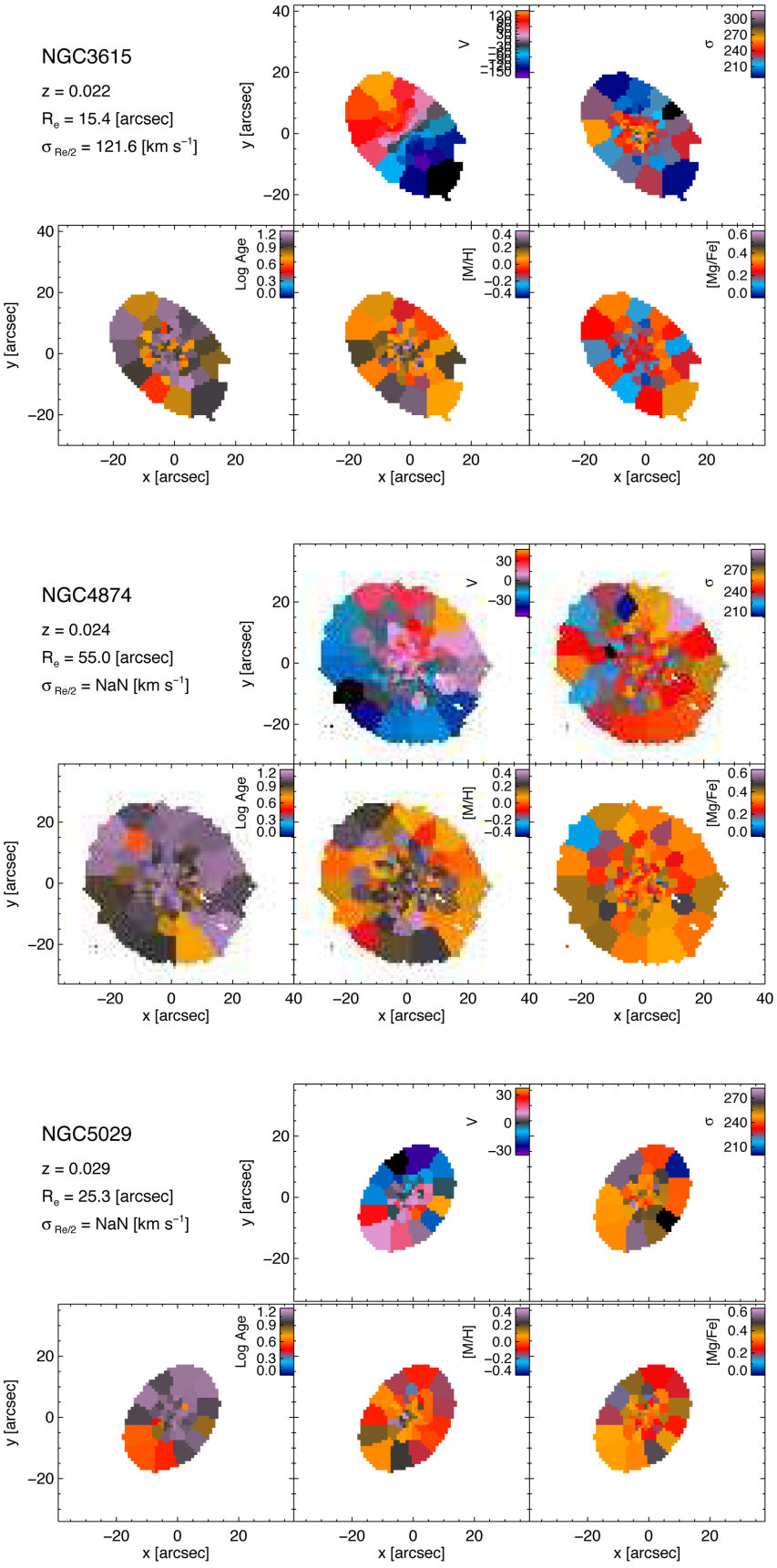

Figure C1 – *continued*

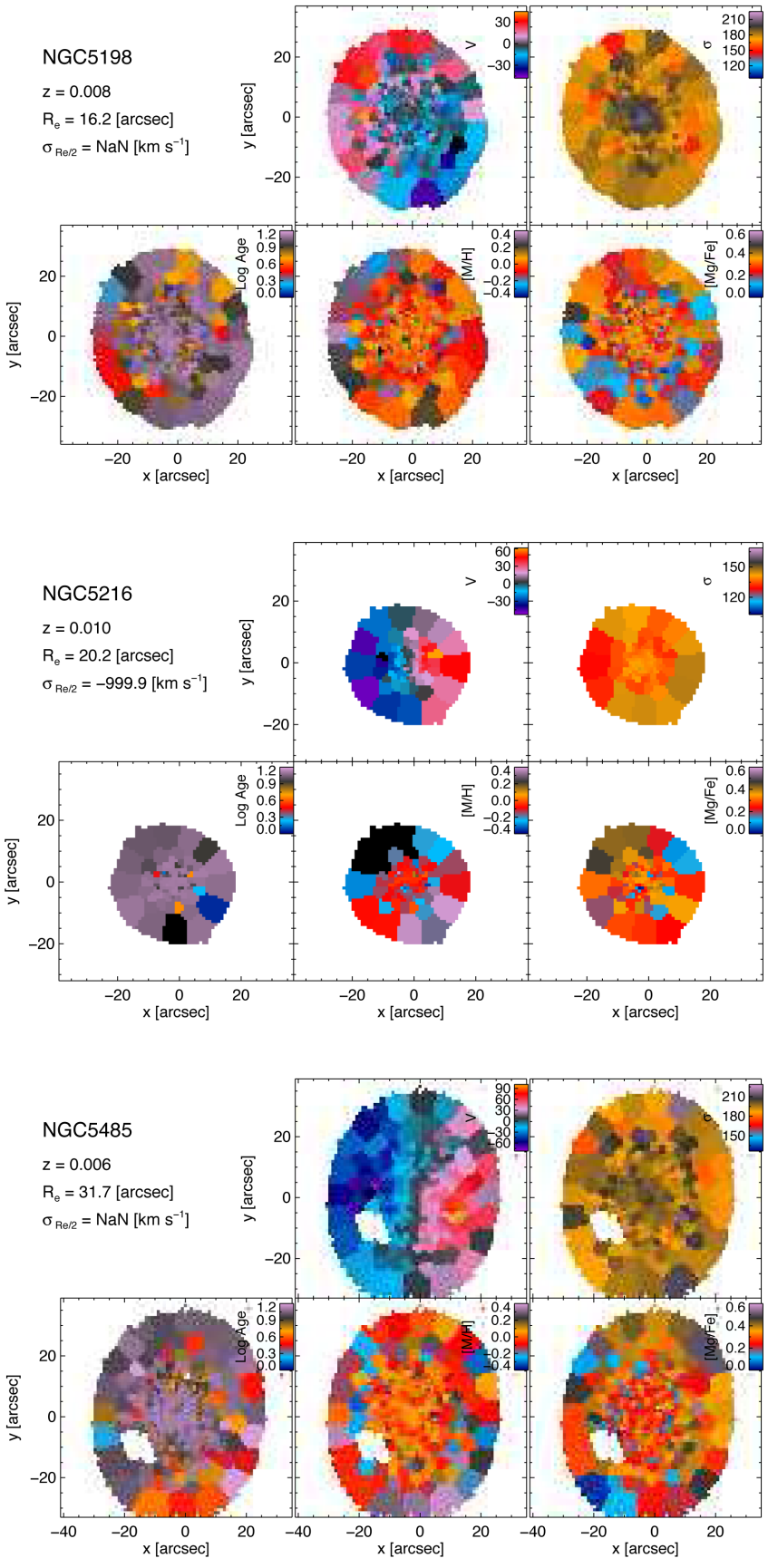

Figure C1 – *continued*

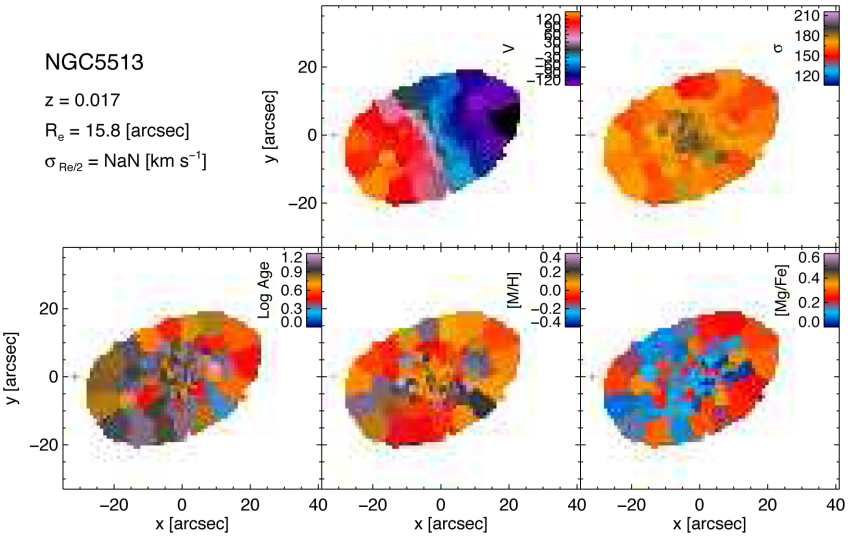

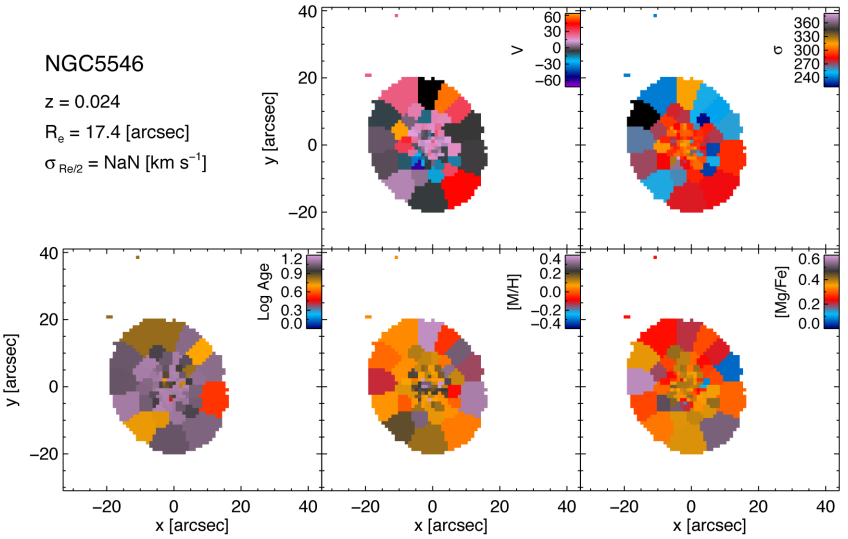

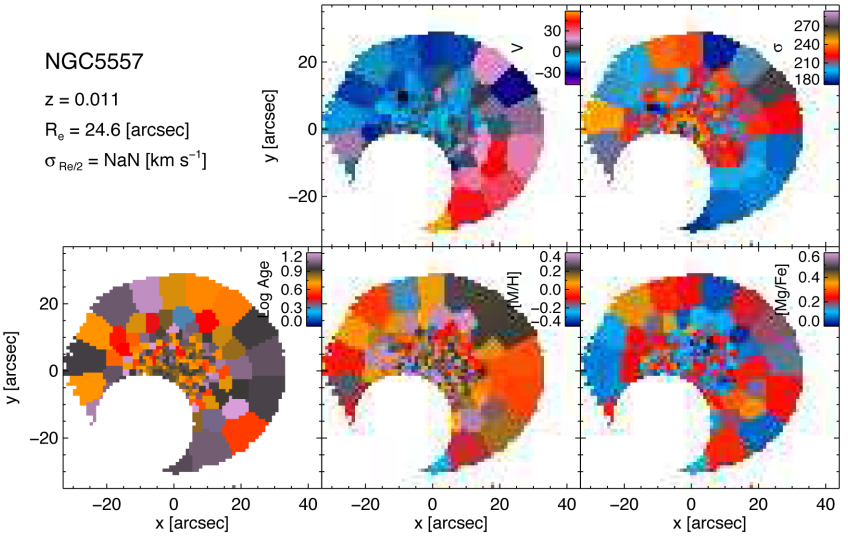

Figure C1 – *continued*

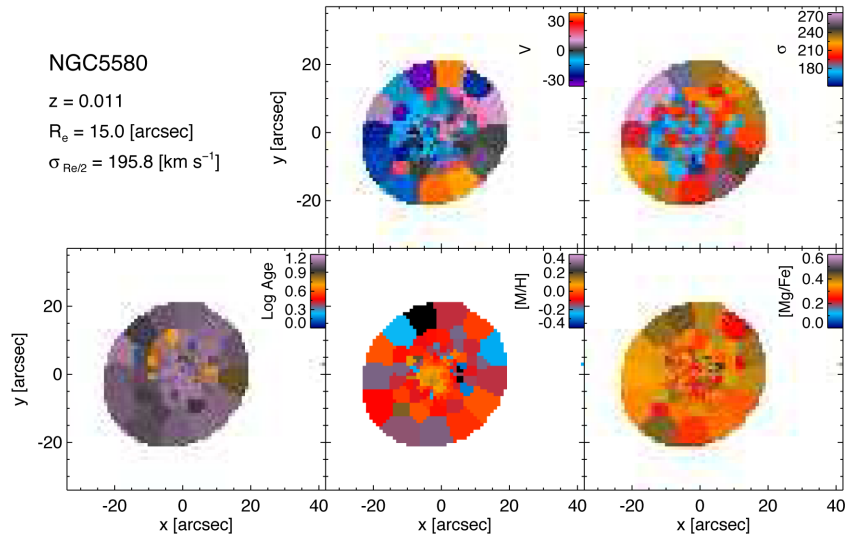

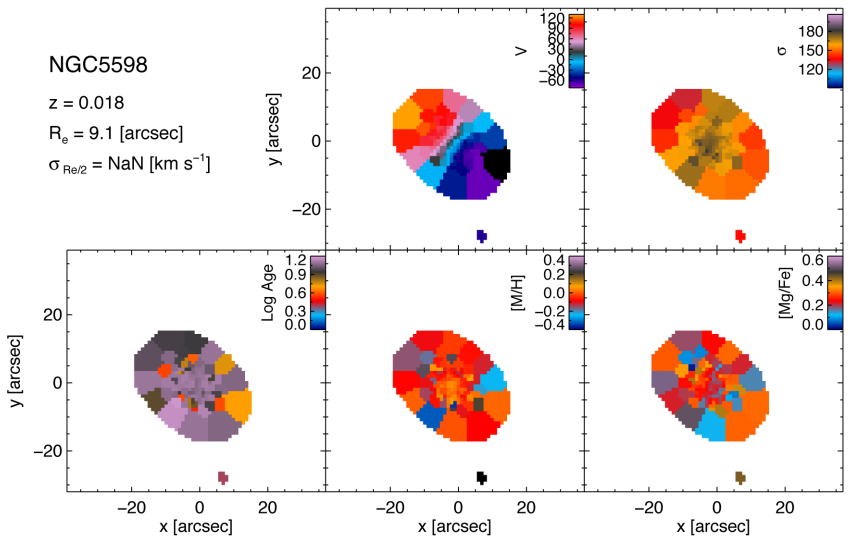

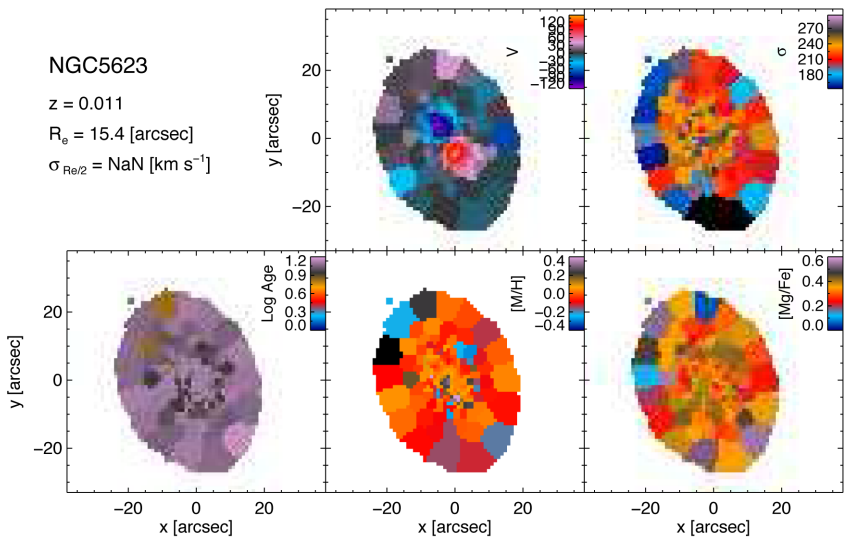

Figure C1 – *continued*

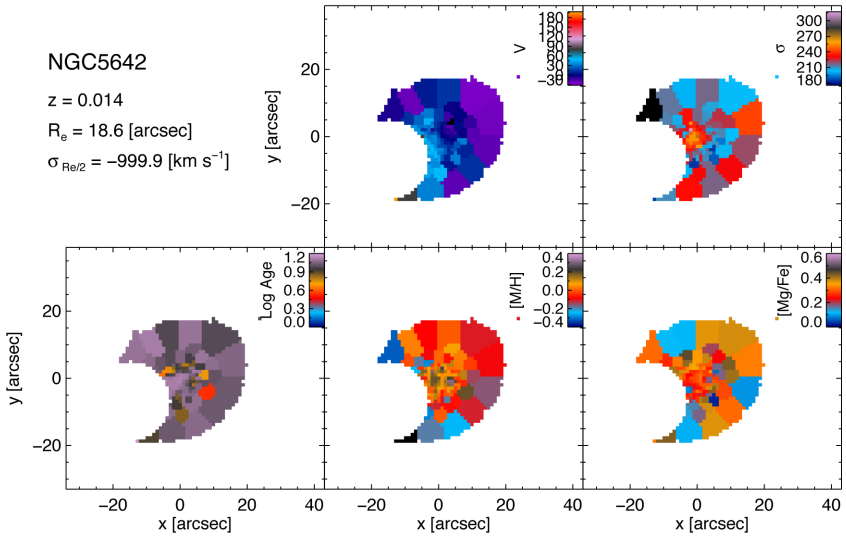

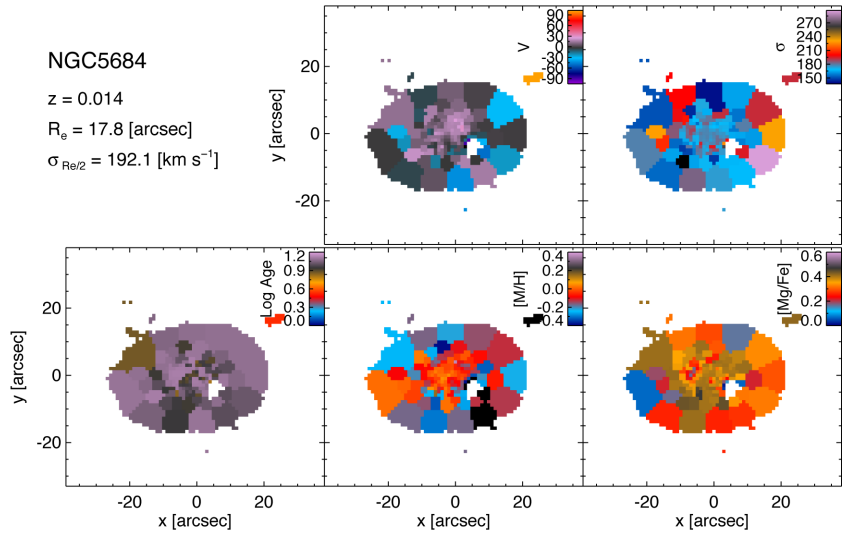

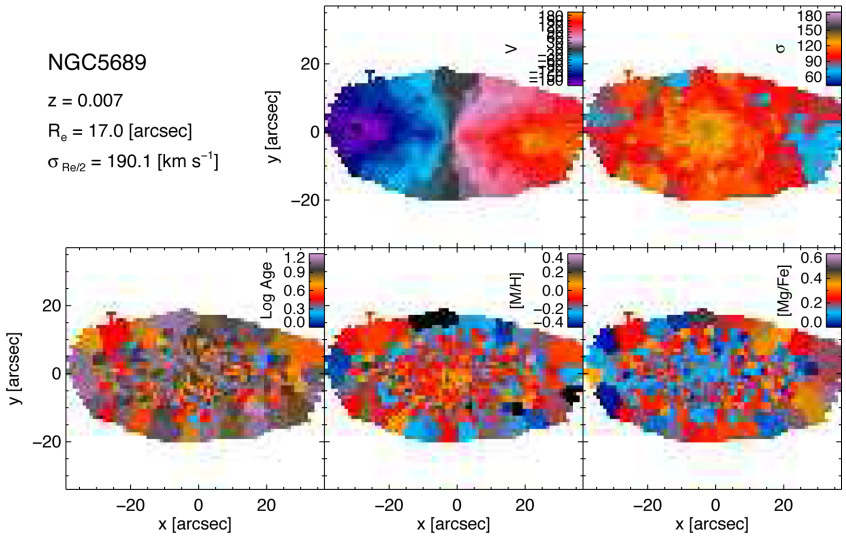

Figure C1 – *continued*

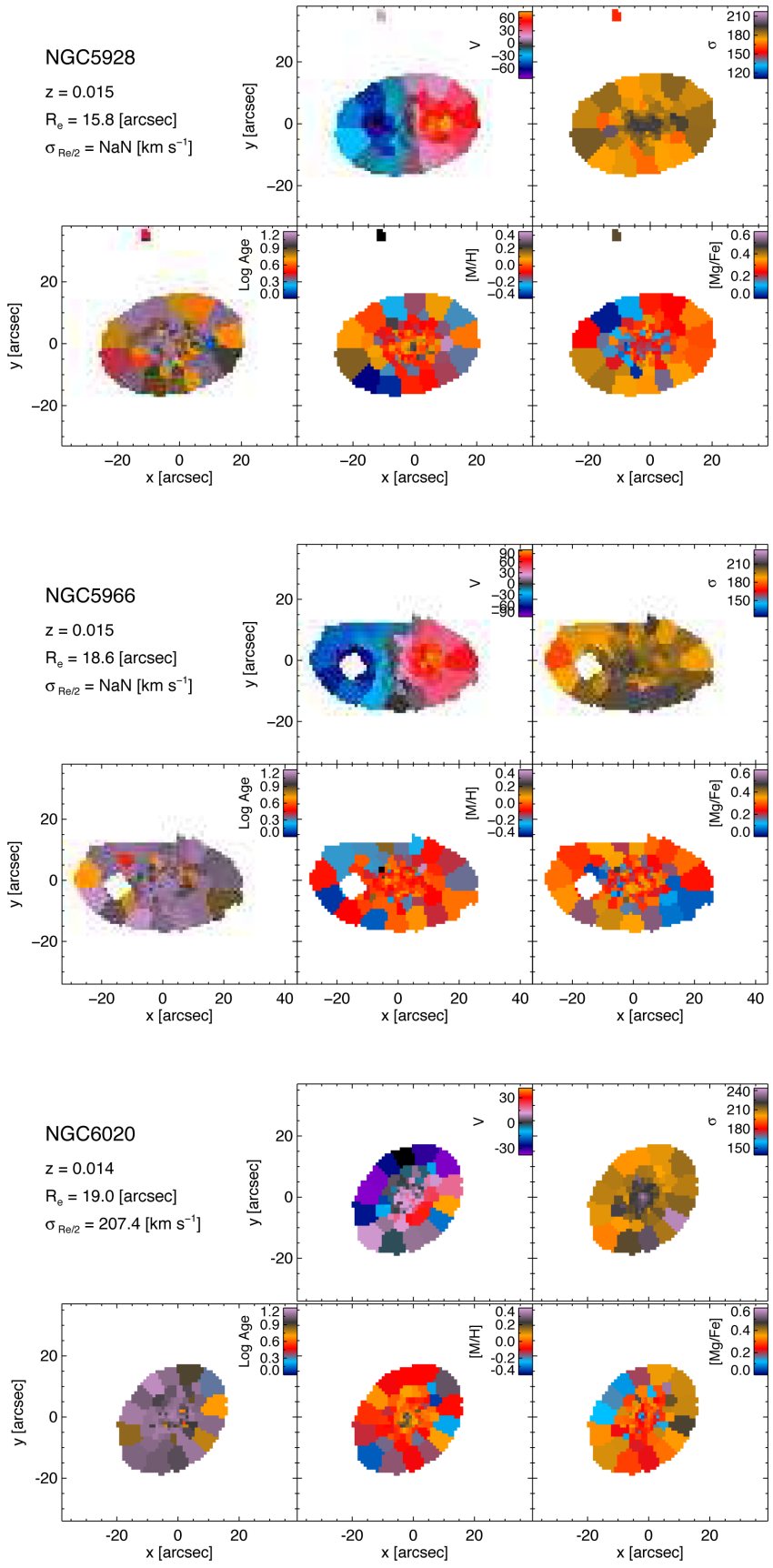

Figure C1 – *continued*

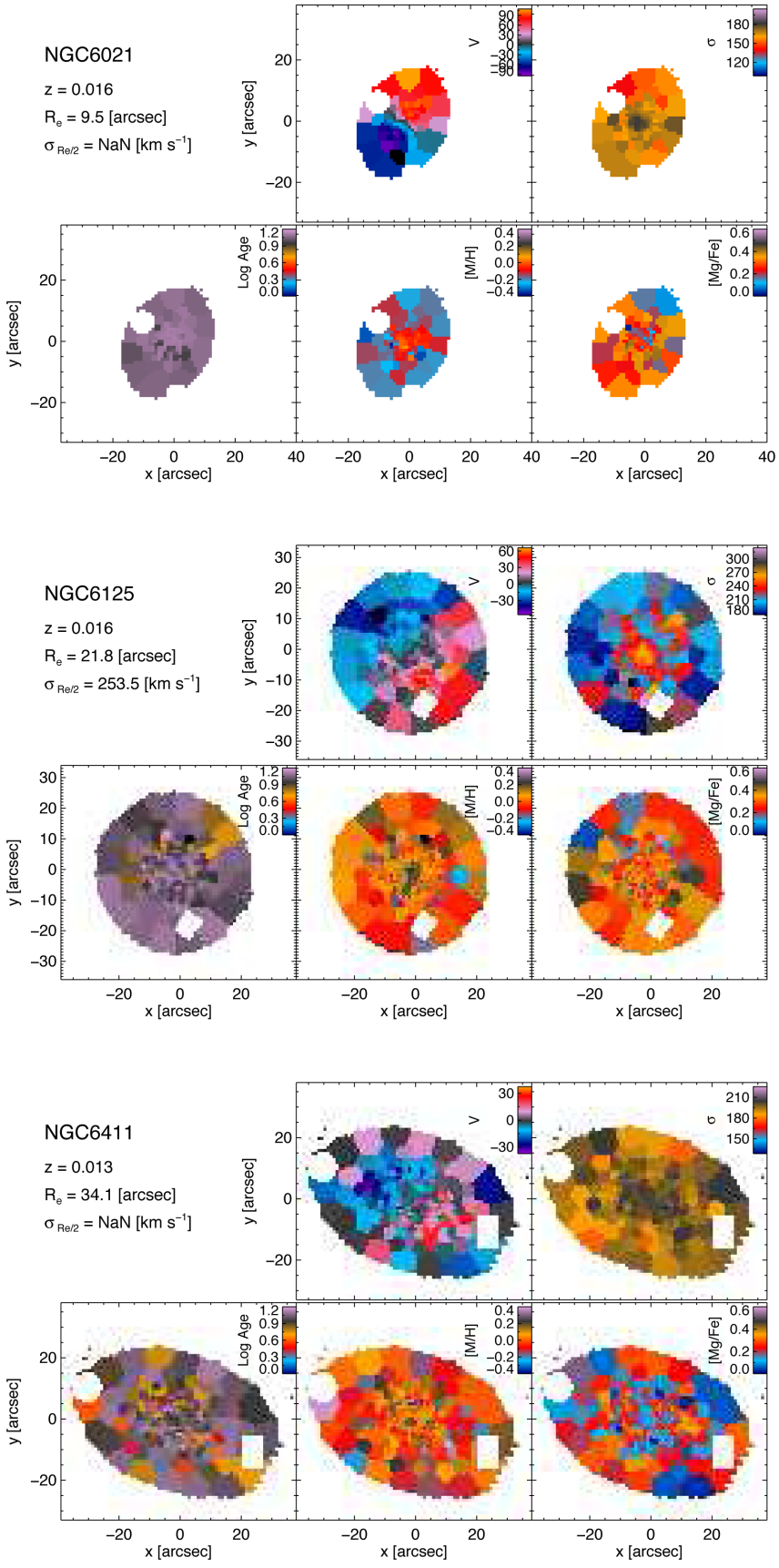

Figure C1 – *continued*

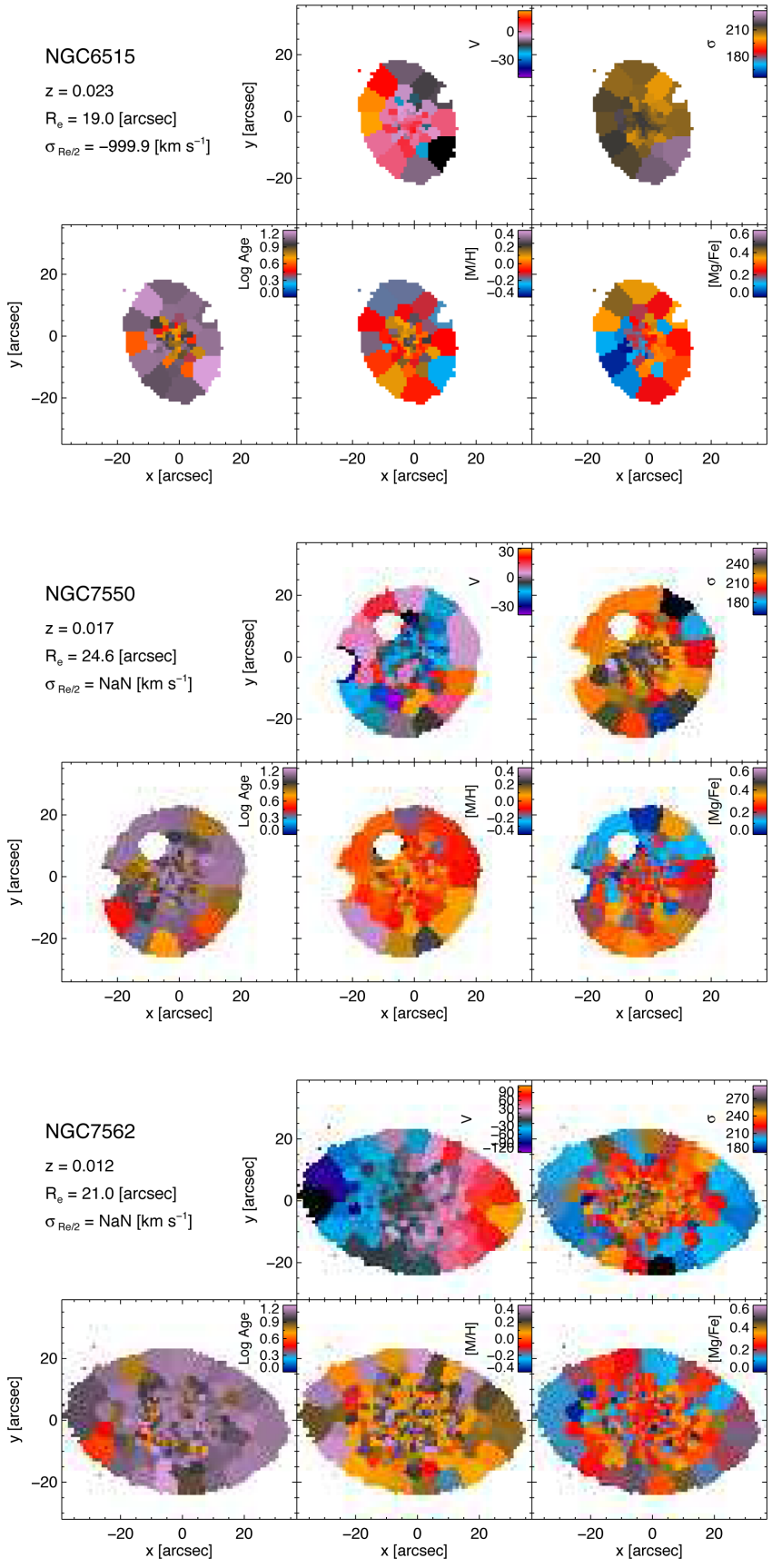

Figure C1 – *continued*

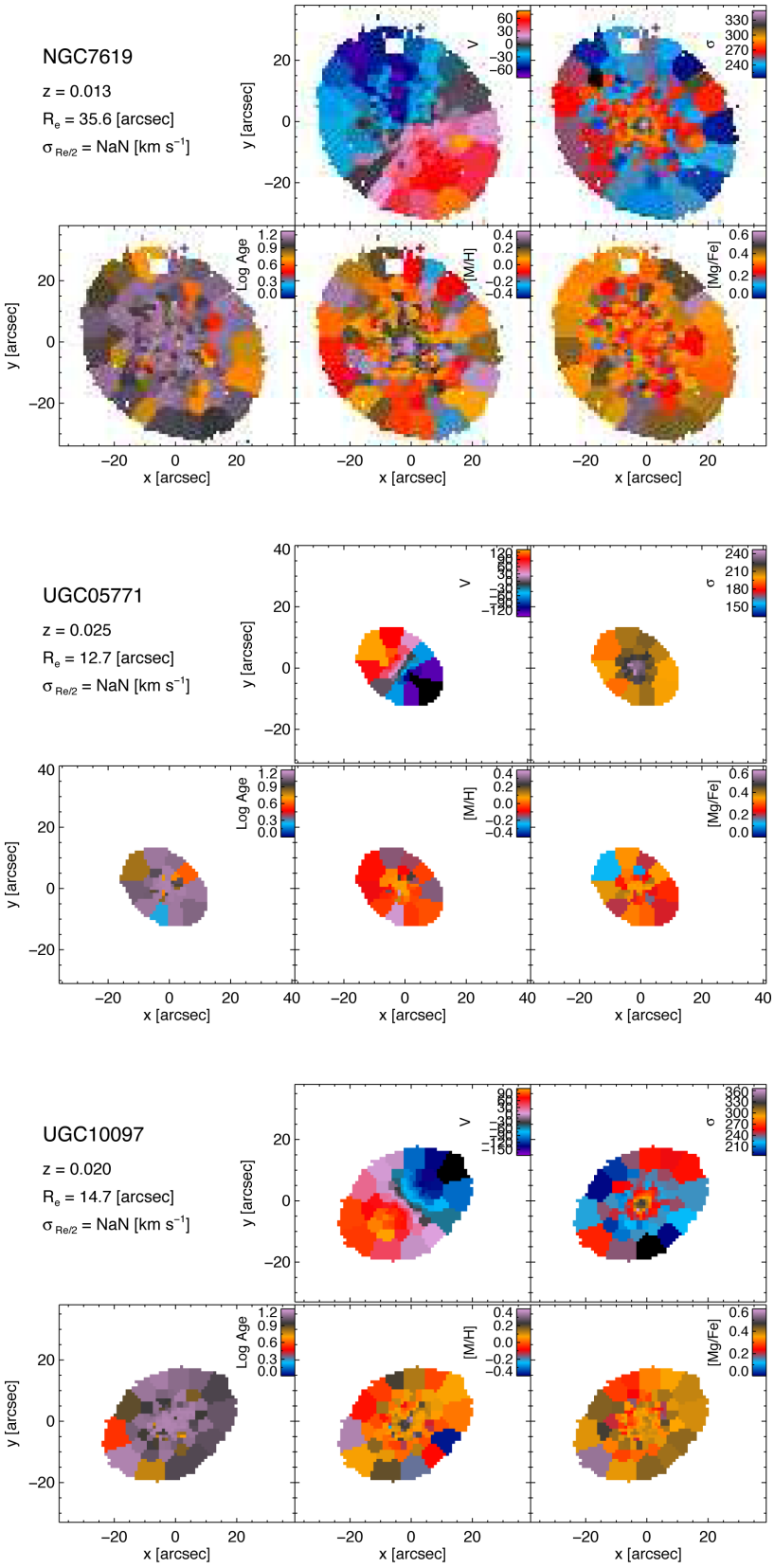

Figure C1 – *continued*

This paper has been typeset from a TEX/LATEX file prepared by the author.